Quasi-geostrophic flows responsible for the secular variation of the Earth's magnetic field

M. A. Pais, Dominique Jault

Quasi-geostrophic flows responsible for the Secular Variation of the Earth's magnetic field

M. A. Pais[1], D. Jault[2]
[1] Physics Department, University of Coimbra, *3004-516* Coimbra, Portugal
[2] LGIT, CNRS, University Joseph Fourier, BP 53, 38041 Grenoble Cedex 9, France

2008 January 8

Abstract

A large jet encircling the inner core and carrying a significant part of the core angular momentum and axial vortices of $\sim$ 700 km diameter mainly clustering around the cylinder tangent to the solid inner core, are inferred from geomagnetic secular variation. These results are presented in the form of maps of axial vorticity in an equatorial section. The study takes advantage of the high precision of recent geomagnetic field models derived from satellite data. The tangent cylinder is considered as impenetrable to core flows and, outside of it, the same eddies account for magnetic field induction at the core surface in both hemispheres. New regularizations are suggested from dynamical considerations. It is found that medium and small scale velocity fields contribute significantly to the large scale secular variation. Accordingly, final models of core flows are calculated after an iterative process, whereby the magnetic field variation produced by small scale stochastic magnetic fields and medium to small scale computed velocity fields are incorporated into the inversion itself as modelling errors. This study represents a significant step in an effort to join geomagnetic observations and the fluid core dynamics on short timescales.

1 Introduction

Recent years have seen rapid advances in the understanding of the Earth's fluid core dynamics, especially since fully three-dimensional dynamo numerical models produced their first results (Glatzmaier & Roberts, 1995). One surprising outcome of these complex numerical calculations is that, in many cases, the well-known dynamical rigidity parallel to the direction of rotation, characteristic of motions in a rapidly rotating system, is still present in spite of convection and magnetohydrodynamic effects (see e.g. Olson et al. (1999)). During the same time, particularly for the last seven years, the three satellites Ørsted, SAC-C and CHAMP have been providing geomagnetic data, in such a way that the overall database covers a $6,5$ yr period continuously (Olsen et al., 2006; Maus et al., 2006; Thomson & Lesur, 2007). Never before had the geomagnetic field been monitored with, simultaneously, such accuracy of individual measurements, global density of observation points and long duration. It is expected that these conditions add up to produce models of the Earth's core Secular Variation (SV) with unprecedented resolution of intermediate temporal and spatial scales. Therefore, this seems to be the right time to put together dynamical results and observations and try to compute Core-Mantle Boundary (CMB) flow models that are compatible with both theoretical and observational constraints.

Experimental and numerical studies of fluid dynamics in rapidly rotating spherical shells are a central issue for the understanding of planetary and astrophysical systems in general, and the Earth's core in particular (Busse, 1976). Columnar flows aligned with the rotation axis, z, have often been seen to emerge in laboratory experiments, as preferred self-organized structures (e.g. Cardin & Olson (1994), Aubert et al. (2001), Gillet et al. (2007)). Columnar axial vortices are the expression of Proudman-Taylor theorem, which applies when the main force balance is dominated by the Coriolis and pressure forces and implies a kind of dynamical rigidity on the fluid parallel to the rotation axis, known as geostrophy (e.g. Tritton (1988)). As a result, a purely geostrophic flow is two-dimensional in the plane perpendicular to the rotation axis. Inside a spherical shell, it corresponds to cylindrical flows, coaxial with the rotation axis, since any z-invariant radial component would violate the impenetrability condition on the boundary. Spherical sloping impenetrable boundaries do impose compression of fluid columns that move radially outward from the rotation axis, and stretching of inward moving columns, thus inducing an ageostrophic (i.e., z-dependent) axial flow component. This geometrical boundary effect is known as topographic β-effect (e.g., Busse (2002)) and the resulting flow is quasi-geostrophic (QG). For studying the dynamics of the Earth's liquid outer core, buoyancy and magnetic forces have necessarily to be included (e.g., Gubbins & Roberts (1987)). These forces can induce radial flows, liable to be affected by the topographic β-effect, and an ageostrophic flow component can be expected. Yet, a number of analytical, numerical and experimental studies on thermal, nonmagnetic, rotating convection, have shown that flows driven by a realistic temperature or compositional gradient are almost two-dimensional, with convective cells aligned with the rotation axis (see Jones (2007), for a review and Zhang et al. (2007) for a reappraisal from the viewpoint of quasi-geostrophic inertial waves). Magnetoconvection numerical studies consider the impact of an imposed magnetic field on convection of an electrical conducting fluid. In most of these studies, the columnar convection still dominates, though rolls become thicker as the magnetic field effect increases (e.g., Jones et al (2003)). Convection-driven numerical dynamos allow for the modification of the ambient magnetic field by the back-reaction of the convective flow. There, also, strongly columnar regimes have been observed, associated to dipole-dominated external fields of the Earth's type (Olson et al., 1999; Christensen & Aubert, 2006). The mechanism by which convective rolls generate magnetic field by dynamo action, is discussed with detail in Olson et al. (1999).

One of us (Jault, 2007) has recently attempted to put these results in a general framework. The study is motivated by the observation that the timescale of interest for SV studies from satellite data is of the order 1-10 yrs. It relies on a numerical calculation with imposed axial symmetry. It is found that the relevant parameter for emergence of geostrophic cylinders when viscous and magnetic diffusive effects can be neglected is the ratio, λ, between the periods of inertial and Alfvén waves in a rotating system permeated by a magnetic field instead of the Elsasser number Λ. Then, it is remarked that magnetoconvection and dynamo studies showing columnar flows aligned parallel to the axis of rotation are all associated to values of λ much smaller than unity $\lambda < 3. \times 10^{-2}$. Hence, it is suggested that λ is the appropriate parameter to measure the relative importance of magnetic and Coriolis forces, even for non-axisymmetric systems. For the Earth's core, $\lambda \sim 10^{-4}$, suggesting a dominance of rotation upon magnetic effects.

Quasi-geostrophic flows have to be distinguished from tangentially geostrophic surface flows (Le Mouël et al, 1985; Jackson, 1997; Chulliat & Hulot, 2000; Pais et al., 2004). The former affect the entire fluid volume where they obey an equation for axial vorticity while the latter are restricted to the core surface where they are constrained by a radial vorticity equation compatible, for example, with a thermal wind balance. Calculations of tangentially geostrophic flows have been justified by the locally small value of the Elsasser number Λ. Acknowledging that λ is more appropriate than Λ to measure Coriolis forces against magnetic forces when magnetic diffusion is negligible, brings out the relevance of QG flows on short timescales.

For CMB flow inversion, the QG assumption has the advantage of eliminating the well-known non-uniqueness of solutions (Backus, 1968) by providing new constraints supported by dynamics. Indeed, the most obvious implication of the underlying dynamics for the kinematics of CMB flows is the equatorial mirror symmetry. It has also been frequently noticed in dynamo calculations (Olson et al., 1999; Christensen & Aubert, 2006; Sreenivasan & Jones, 2006), a decoupling of the flow inside and outside the cylinder coaxial with the rotation axis and which touches the inner core equator, usually called the tangent cylinder (TC). This result can be explained in the light of a dynamical regime controlled by rotation, by stressing that the rapid change in length of columns that cross the TC requires a strongly ageostrophic motion of which there would be no source mechanism (Jones , 2007). A further implication is that length scales associated to columnar flows are expected to be smaller than those dominating standard CMB inverted flows, because tall thin columns minimize the violation to the impenetrability condition at the spherical core surface and, accordingly, the departure from geostrophy induced by the boundaries (e.g., Busse (1970)). As a summing up, we can say that dynamical arguments favour i) equatorial mirror symmetry; ii) minimum fluid transfer through the TC; iii) relatively short length scales for the flow.

A review of core-mantle flow modelling from inversion of geomagnetic data, with discussion of the main aspects related to this procedure, is given by Whaler & Davis (1997) for the classical spectral approach. We elaborate now on points i), ii) and iii) referred above, where our inversions differ from the usual procedure.

Hulot et al. (1990) computed a tangentially geostrophic CMB flow for epoch 1980, imposing symmetry about the center of the Earth and plane reflexion symmetry (or mirror symmetry) about the equatorial plane. They could resolve different vortices, of large diameter $d \sim 7000$ km, which they interpreted as the surface expression of columnar flows. Using models derived from satellite data, Hulot et al. (2002) inverted a mean MF/SV model over the 20 yr period that separated Magsat from Ørsted satellite missions and reported a medium to high-latitude ring of vortices, approximately symmetrical with respect to the equator. Also, Holme & Olsen (2006) noticed a strong equatorial symmetry in surface core flows inverted from a geomagnetic field model, CO2003, determined from the Ørsted and CHAMP satellite data covering a 4.5yr period. They related these highly symmetrical features to the convective features described by Busse (1970). Note that this conclusion of both Hulot et al. (2002) and Holme & Olsen (2006) contrasts with the remark of Amit & Olson (2004) that their core flows inferred from the variation of the magnetic field between the epochs of Magsat and Ørsted show little evidence of non-axisymmetric Taylor columns. Amit & Olson (2004, 2006) relied on studies of other geophysical flows to suggest new ways to invert for core flows. Their helical and columnar flows hypotheses are used only to infer certain conditions on the CMB flow that eliminate the associated non uniqueness. The flows are defined at the core surface alone and no symmetry with respect to the equator is imposed. Previous studies, using magnetic observatory data, had identified some important equatorially asymmetric features in the computed flows, such as the strong westward drift under Africa and under the South Atlantic and the gyratory flow below the Indian ocean (e.g. Bloxham, 1989). Rau et al. (2000) inverted the secular variation from numerical dynamo models and compared the inverted flows to flows extracted from the numerical model, below the outer Ekman boundary layer. They pointed out that the usual pattern seen in standard inverted flows, namely strong westward currents within 30^o latitude and large gyres that do not close locally into complete vortices, may well be a spurious effect of limited resolution of the MF and SV, blurring an underlying equatorial symmetric, columnar flow.

To our knowledge, the tangent cylinder has not yet been explicitly introduced in core flow inversions. However, a possible influence of that imaginary cylinder on core flows has been sought, either by direct inspection of core flow maps (Pais & Hulot, 2000; Hulot et al., 2002; Holme & Olsen, 2006), or by examination of high latitude distribution of magnetic field time variations (Olson & Aurnou, 1999). All these studies concluded that a large polar vortex is present at the North Pole. Another polar vortex with possibly a weaker amplitude has also been inferred at the South Pole from plots of the zonal toroidal velocity component as a function of latitude. Finally, the high latitude ring of vortices of Hulot et al. (2002) clusters around the tangent cylinder.

Hulot et al. (2002) have been the first to use high precision satellite data to inspect intermediate to small length scales of the CMB flow. The smallest high latitude vortices obtained by these authors from inversion of Magsat to Ørsted field changes in the Atlantic hemisphere, have a diameter of about 1000 km. Holme & Olsen (2006) inverted the CO2003 model truncated at degree 14 for more detailed flow images at the CMB. Their computed flows show much more small scale structure than previously published flows. In both studies, flows were strongly regularized. Nonetheless, they didn't show a clear convergence at the truncation degrees 13 (Hulot et al., 2002; Eymin & Hulot, 2005) nor 14 (Holme & Olsen, 2006), suggesting that a higher truncation degree should be used. When trying to assess smaller scale flows, as pointed out by Eymin & Hulot (2005), we are confronted with a crucial limitation of the inversion model, as we have to deal with only a partial knowledge of the main field. This discussion is expanded in section 3.

The aim of this paper is to investigate the possibility that secular variation, continuously monitored by satellites since only a few years ago, is due to advection of the geomagnetic field by QG vortices. The features of our method that are in common use are expounded in section 2, together with a discussion of available data. In section 3, we explain how we estimate modelling errors to invert for flows in a self-consistent way. In section 4, we describe the kinematics of a QG flow model inside the core, and derive the expressions to describe its core surface signature. In section 5, we present the different kinds of constraints used in the inversion. Section 6 is for the presentation of results, conclusions and discussion are presented in section 7.

2 Inversion of geomagnetic data

2.1 Data

Recent models for the near-Earth magnetic field, such as CHAOS (Olsen et al., 2006) and POMME3 (Maus et al., 2006), have been derived using high-precision satellite data from Ørsted, CHAMP and SAC-C satellites in the former case, and only CHAMP satellite in the latter case. A special emphasis has been given to the fact that a precise monitoring of geomagnetic field variations during a 6.5 yr and a 5 yr time periods, respectively, might translate into resolution of small time and spatial scales with unprecedented accuracy. Although CHAOS SV model is considered reliable up to spherical harmonic degree 15 (Olsen et al., 2006), a relatively flat tendency in the corresponding Mauersberger-Lowes spectrum curve can be easily identified above degree 13 (fig. 2 from (Olsen et al., 2006)). This flat tendency is usually associated to the emergence of the noise level (see e.g. (Maus et al., 2006)) and the reason why it is absent from the POMME3 SV model is the imposed damping of degrees $n \geq 14$. Finally, we note that presently available main field models derived from satellite data significantly underfit the field variations as it has just been shown for the CHAOS model by Olsen & Mandea (2007) (see their Figure 3). As to the main core field, it is well-known that, while dominating at long wavelengths, it is masked by the crustal field above spherical harmonic degree 14 (e.g., (Langel & Estes, 1982)). Global crustal magnetic field models computed from satellite magnetic measurements rely on data subtracted from an internal field model up to degree 14 or 15 (Maus et al., 2006), and will inevitably also include the short length scales of the core field. Accordingly, and at the present stage, they can't be used to extract the crustal field from the total geomagnetic field data.

In our study we use CHAOS as MF and SV models, both truncated to degree 13, and concentrate on the equally spaced epochs 2001.0, 2002.5 and 2004.0, avoiding the edges of the model time interval, where spurious effects from using cubic B-splines can show up. We also consider SV models from POMME3 as alternative realizations to CHAOS SV models for corresponding epochs. We then use as a conservative estimate of the SV error the differences between CHAOS and POMME3 which we subsequently refer to as the "pessimistic" SV uncertainties. As another possible estimate of the SV error, though probably too optimistic, we use the noise level of 0.02 nT^2/yr^2 appearing in the SV spectrum for CHAOS, at the model middle epoch 2002.5 (Olsen et al., 2006), hereinafter referred to as the "optimistic" SV uncertainties.

2.2 The regularized least squares approach

The formalism and notation is the same as in Pais et al. (2004) and is rather standard in conventional flow inversion spectral methods (see Whaler & Davis (1997) for a review). The Helmholtz representation of the tangential velocity $\mathbf{u}_H$ in terms of poloidal $\mathcal{S}(\theta,\phi)$ and toroidal $\mathcal{T}(\theta,\phi)$ components is:

$$\mathbf{u}_H(\theta,\phi) = r_c \nabla_H \mathcal{S} - r_c\ \hat{\mathbf{r}} \wedge \nabla_H \mathcal{T} \qquad , \tag{1}$$

where r_c is the core radius, (r,θ,ϕ) are spherical angular coordinates and $\nabla_H = \nabla - \hat{\mathbf{r}}\partial/\partial r$ is the horizontal gradient operator on a spherical surface. We use $(s_n^{m,c}, s_n^{m,s})$ and $(t_n^{m,c}, t_n^{m,s})$ for the degree n, order m poloidal and toroidal spherical harmonic coefficients of the flow under the Schmidt semi-normalization of the associated Legendre functions. Using the same normalization, the main magnetic field $\mathbf{B}$ and its SV are described in terms of the spherical harmonic coefficients (g_n^m, h_n^m) and $(\dot{g}_n^m, \dot{h}_n^m)$, respectively.

Truncating the main field and the SV at $n = L_B$ and $n = L_y$, respectively, and the flow at $n = L_x$ and substituting into the frozen-flux radial induction equation at the core surface,

$$\frac{\partial}{\partial t} B_r = -\nabla_H \cdot (\mathbf{u}_H B_r) \qquad , \tag{2}$$

gives the linear equation

$$\mathbf{A}\mathbf{x} = \mathbf{y}\ , \tag{3}$$

where $\mathbf{y}$ is the vector of the $(\dot{g}_n^m, \dot{h}_n^m)$ SV Gauss coefficients, $\mathbf{x}$ is the vector of the $t_n^{m,c(s)}$ and $s_n^{m,c(s)}$ flow coefficients, and $\mathbf{A}$ is the interaction matrix whose elements account for the importance of each elementary flow in generating each coefficient of the SV.

The method used in this study relies on the Regularized Least Squares (RLS) criterion, where an estimate $\hat{\mathbf{x}}$ is sought that minimizes the objective function

$$\Phi(\mathbf{x}) = (\mathbf{A}\mathbf{x} - \mathbf{y})^T \mathbf{C}_{\mathbf{y}}^{-1} (\mathbf{A}\mathbf{x} - \mathbf{y}) + \sum_i \lambda_i \mathbf{x}^T \mathbf{C}_i^{-1} \mathbf{x} \qquad . \tag{4}$$

In the expression above, the first term on the right is a least squares discrepancy between data and model estimation, normalized by the covariance matrix for the secular variation, $\mathbf{C}_{\mathbf{y}}$. The terms $\mathbf{x}^T \mathbf{C}_i^{-1} \mathbf{x}$ are the regularization norms and λ_i are the corresponding penalization parameters. This method is suitable to accommodate the *a priori* on the core flow that are discussed in section 5.

3 Taking into account under-parameterization of the MF and of the flow

3.1 Effect of MF small scales

There is no point in trying to achieve a very small misfit $M = \sqrt{(\mathbf{A}\mathbf{x} - \mathbf{y})^T (\mathbf{A}\mathbf{x} - \mathbf{y})}$ when inverting for CMB flows, since it is well known that i) errors in SV coefficients due to observational and modelling limitations (e.g. Pais & Hulot (2000)); ii) under-parameterization of the MF and of the inverted flows related to the use of truncated series (Hulot et al., 1992; Celaya & Wahr, 1996; Rau et al., 2000; Eymin & Hulot, 2005); iii) inability of the model to treat the effects of diffusion (Holme & Olsen, 2006), are to be expected. Nevertheless, it is possible to estimate the effects due to each one of these unavoidable error sources, and simply accept that the inverted flow solutions can explain the observed SV only up to the uncertainty level of the estimated errors. This amounts to tuning the penalizing parameters λ_i in (4) in such a a way that

$$\chi = \sqrt{\frac{\left(\mathbf{Ax} - \mathbf{y}\right)^T \mathbf{C}_\mathbf{y}^{-1} \left(\mathbf{Ax} - \mathbf{y}\right)}{N_y}} \sim 1 \tag{5}$$

χ is the normalized weighted misfit, N_y is the number of spherical harmonic coefficients used to describe the SV and $\mathbf{C}_\mathbf{y}$ is the covariance matrix, properly modified to a form which more accurately accounts for all error sources and in particular unsolved-for parameters.

Though this has been the usual approach when dealing with SV errors (item i), see e.g. Pais & Hulot (2000), it is not usually done for the other two error sources in CMB flow computations. In this study, we focus on error source ii) and follow Holme & Olsen (2006) in quantifying error source iii).

Hulot et al. (1992) estimated the contribution of high degree terms of the MF and of the flow to the observed large scales of SV, in the frozen-flux approximation. Critical to their study are the assumptions made on the statistical properties of the flow, which require that the spectrum of the flow decays with n^{-2}. Celaya & Wahr (1996) considered the problem of spatial but also temporal under-parameterization of the flow in frozen-flux core-surface flow inversions. They tested synthetic flows with different energy spectra and different time variations, to finally conclude that only if the spectra fall off as n^{-2} or faster, and the steady-motion constraint is relaxed, can under-parameterization effects (aliasing) be neglected. Whether these conditions are satisfied or not by CMB real flows is, of course, a completely different issue. Rau et al. (2000) and recently Amit et al. (2007), could test different inversion assumptions using core flows taken from self-consistent 3-D dynamos calculated for high values of the Ekman number (compared to what is presently achievable) and producing dipole-dominated fields. They identified as a main problem that, in case the numerical model core flow contains substantial energy at intermediate scales, the resolution below degree 14 of the magnetic field would produce serious artifacts of the computed flows. These artifacts would be seen even at long flow wavelengths. Eymin & Hulot (2005) estimated the SV induced by unresolved small-scale flows interacting with both the known and the unknown scales of the MF and by large-scale flows interacting with the unknown small-scale magnetic field, which they called non-modelled secular variation. They tested different *a priori* extrapolations of the flow spectra and used a reasonable extrapolation for the MF spectra. They also identified as the main source of non-modelled secular variation, the lack of knowledge of the small scales of the MF (components above degree 14).

The MF spectrum at a certain distance r from the Earth's center, in a region where the field is irrotational, is given by $R(n) = (n+1)(a/r)^{2n+4} \sum_{m=0}^{n} \left[(g_n^m)^2 + (h_n^m)^2\right]$, where a is the Earth's reference radius, taken as 6371.2 km. Following Langel & Estes (1982) and Eymin & Hulot (2005), we use as a model for the non-dipole observational

MF spectrum at the Earth's surface the simple formula

$$R^*(n) = R^0 \left(\frac{r'}{a}\right)^{2n+4} \qquad , \tag{6}$$

corresponding to a straight line in a semilogarithmic graph, with R_0 in nT^2/yr^2 and r' in km (see Voorhies et al. (2002) for a somewhat more complex core-source magnetic spectrum). We derive the two parameters (R^0, r') from all the MF coefficients from $n = 2$ to $n = 13$, by using a least square procedure, for epochs 2001.0, 2002.5 and 2004.0. The values $(14 \times 10^9, 3.39 \times 10^3)$ apply for the whole time interval. The extrapolation of the MF spectrum to degree $L_B = 30$ assumes that model $R^*(n)$ describing the behaviour of the MF that can be known, remains valid for degrees larger than 13. We adopt an isotropic statistical model for the non-dipole field, where the set $\{g_n^m, h_n^m\}$ of non-dipole coefficients are treated as independent Gaussian centered variables (e.g. Eymin & Hulot (2005)). We thus use a zero mean Gaussian random generator, with the variance σ_n^2 associated to each degree $n > 13$ coefficient given by

$$\sigma_n^2 = \frac{R^*(n)}{(n+1)(2n+1)} \qquad .$$

With this statistical model for the small scale magnetic field (BS), we can gauge the SV produced by BS interacting with a core surface flow model, as done by Eymin & Hulot (2005). In all computations, we use truncation of flow scalar series at the maximum degree, $L_x = 26$, that can be constrained (even if only slightly) by the first 13 degrees of the MF and of the SV, on account of the triangle rule applying for the interaction integrals used to compute the elements of matrix $\mathbf{A}$ (e.g. Hulot et al. (1992)). Figures 1a) and 1b) refer to a tangentially geostrophic flow, $\hat{\mathbf{x}}_1$, computed in a standard way (e.g. Pais et al. (2004)) for 2001.0, using as data only the first 8 degrees of CHAOS SV model (Figure 1a, solid line). The variance attributed to these SV coefficients conforms to the 'pessimistic' perspective (Figure 1a, circle-dashed line) and the standard strong regularization of Bloxham (1988) was used, in order to ease the comparison with other studies. Only the large scale and known magnetic field (BL) contributes to the elements of the interaction matrix $\mathbf{A}$. The choice of the attenuation parameter λ (the Lagrangian multiplier applied to the regularization norm, see eq. (4)) was determined by $\chi = 1.0$. As we can see in Figure 1b), where the mean energy per degree of poloidal (grey diamonds) and toroidal (black circles) coefficients is represented, only the first 10 or 11 degrees of the inverted flow are constrained by the SV coefficients, the knee in the spectrum showing the degree above which the solution is constrained by the regularization alone. Figure 1a) shows that the misfit errors (star-dashed line) are in accordance with the precision attributed to the data. But Figure 1a) also shows that the SV produced by this flow interacting with BS (dot-dashed line) is much a more important signal. The situation is even more critical if we compute a flow that explains the SV model up to degree 13, attributing the same 'pessimistic' uncertainty to the CHAOS model coefficients. Then, as shown in Figure 1d), smaller flow scales are required, up to about degree 16, and only for higher degrees does regularization effects prevail. By advecting BS, such flow can produce a SV signal much higher than the uncertainty attributed to the model coefficients. These results unveil an internal inconsistency that we propose to eliminate.

3.2 Iterative estimation of the modelling error

Using two different sets of damping parameters λ_i (see eq. 4), we compute two different flow solutions, 1) and 2), truncated at the same degree, that both account well for the observed SV. These are 1) flow $\hat{\mathbf{x}}_1$, obtained using the known MF up to degree 13 and 2) flow $\hat{\mathbf{x}}_2$, obtained using the observed MF up to degree 13 and an extrapolated BS from degree 14 to degree 30. We use the two solutions 1) and 2) to iteratively calculate $\hat{\mathbf{x}}_1$, as we explain in the following (see also the chart displayed in Figure 2). We start with the covariance matrix $\mathbf{C_y}^{(0)}$, defined with diagonal elements given by an estimation of SV observational errors. Let $\mathbf{y}_1^{(0)} = \mathbf{A}_1\,\hat{\mathbf{x}}_1^{(0)}$ be the SV induced by flow 1) advecting the MF up to degree 13 and $\mathbf{y}_2^{(0)} = \mathbf{A}_2\,\hat{\mathbf{x}}_2^{(0)}$ be the SV induced by flow 2) advecting the known MF but also the extrapolated smaller scales up to degree 30. The secular variation recovered from the two flows are similar, $\mathbf{y}_1^{(0)} \sim \mathbf{y}_2^{(0)}$, within the uncertainty expressed by the covariance matrix $\mathbf{C_y}^{(0)}$. Let us now compute the SV induced by advection of the known part of the MF by $\hat{\mathbf{x}}_2^{(0)}$, i.e., $\mathbf{y}_2'^{(0)} = \mathbf{A}_1\,\hat{\mathbf{x}}_2^{(0)}$. At this point, we have a guess of how different from $\mathbf{A}_1\,\hat{\mathbf{x}}_1^{(0)}$ can be the SV signal resulting from interaction of the flow with the (known) large scale MF, when our model incorporates more information on the MF small scales. The difference

$$\mathbf{y}_1^{(0)} - \mathbf{y}_2'^{(0)} \tag{7}$$

gives us an estimate of the error on SV due to our ignorance of the small MF scales (BS). We fit a straight line to the mean difference per degree, and use this as an estimate of the modelling errors in SV due to under-parameterization of the MF, assumed isotropic. We compare these modelling errors with the corresponding diagonal elements of $\mathbf{C}_\mathbf{y}^{(0)}$, and construct a modified $\mathbf{C_y}^{(1)}$ with the highest of corresponding errors. Note that we use the same covariance matrix $\mathbf{C_y}^{(1)}$ to calculate the flows $\hat{\mathbf{x}}_1^{(1)}$ and $\hat{\mathbf{x}}_2^{(1)}$ so that the calculated modelling error obtained from the difference between the recovered secular variation signals $\mathbf{y}_1{}^{(1)}$ and $\mathbf{y}_2{}^{(1)}$ would be zero for vanishing small scale magnetic field. The new covariance matrix is used in the next iteration, and all the process repeated, until $\mathbf{C}_\mathbf{y}^{(i)}$ does not change from one iteration to the other. At this stage, say iteration $i = k$, the computation has converged for flow solutions $\hat{\mathbf{x}}_1^{(k)}$ and $\hat{\mathbf{x}}_2^{(k)}$, which are both consistent with the SV errors represented by $\mathbf{C}_\mathbf{y}^{(k)}$. The reasoning we rely on assumes that the essential features of small MF scales can be assessed with the MF truncated at degree 30.

In Figures 3 and 4, we show how this procedure modifies the flow solutions previously shown in Figure 1. First, in Figure 3, we show that the prediction from converged flows 1) and 2) are close to each other, but at a distance to the CHAOS model clearly higher then the initial error. The difference between the signal produced by flow 1 and flow 2 advecting BL, is $\mathbf{A}_1\hat{\mathbf{x}}_1 - \mathbf{A}_1\hat{\mathbf{x}}_2$, very similar to the signal due to flow 2 advecting BS, computed from $(\mathbf{A}_2 - \mathbf{A}_1)\hat{\mathbf{x}}_2$. Either one can be used to estimate the modelling error, that is also shown. In Figure 4, we show how the inconsistency appearing in Figure 1 was corrected. Small flow scales were iteratively constrained to produce a lower large scale SV signal. From comparison of the spectra obtained before and after iterative estimation of the modelling error (continuous lines and circles/diamonds, respectively, in Figures 4b) and 4d)), we can describe the effect of this procedure on the final flow as a small shift to lower degrees of the regularization effect, while the spectra are slightly reshaped. Now, the misfit obtained with the converged flow 1 is consistent with the modelling error used as an estimation for the distance of prediction to data.

Two important results can be outlined. Firstly, the slope changes in the spectra (see Figures 4b) and 4d)) mark the degree up to which the flow model coefficients are constrained by the data. It stands out that SV model coefficients between degrees 8 and 13 require more small scales than below degree 8. Secondly, the iterative procedure deteriorates significantly the misfit to the SV model. This is the price to pay to compute flows in a model space limited by our actual knowledge of the MF (flows 1), which are nevertheless consistent with flows computed in a larger, reasonably extrapolated, model space (flows 2).

3.3 Effect of regularization and initial errors on the converged flow

To further illustrate the method using standard regularizations, we consider the computation of tangentially geostrophic flows for 2001.0 when minimizing the kinetic energy of the surface flow (weak regularization) or the second derivatives of the surface flow (strong regularization) (see e.g. Pais et al. (2004)). In this case, a single λ value is to be considered for each inversion 1) and 2), which is chosen to guarantee that the converged $\hat{\mathbf{x}}_1$ and $\hat{\mathbf{x}}_2$ give a χ value of 1.0. The evolution, during the iterative process, of the straight line fitted to the mean modelling SV error per degree, is represented in Figure 5. The black circles correspond to the initial errors in the diagonal of $\mathbf{C}_{\mathbf{y}}^{(0)}$, the dashed line to the first iteration errors in the diagonal of $\mathbf{C}_{\mathbf{y}}^{(1)}$ and the solid line to the converged errors in the last iteration matrix $\mathbf{C}_{\mathbf{y}}^{(k)}$. In Figure 5, we also show the effect of regularization and of the initial errors specified for each SV harmonic degree: while the left column refers to results obtained when using the strong regularization, the right column shows results when using the weak regularization; the first line is for computations starting from 'pessimistic' and the second line from 'optimistic' initial SV error estimations. As we can tell from Figure 5, small scale flows advecting BS do contribute significantly to large scale secular variation, thus increasing the intercept of the final modelling error straight line (solid black lines). As might be expected, the weak regularization amplifies this effect by allowing smaller flow scales to appear. But using very small values for the initial specified SV errors has an analogous, though more tenuous, effect. It suggests that trying to explain the SV data very closely from the beginning requires an important contribution from small flow scales, and that these are kept in all the following iterations.

Following Holme & Olsen (2006), we also represent in Figure 5 the estimate of diffusion effects based on the free-decay modes of the conducting core, assumed spherical and surrounded by an insulating mantle (e.g. Roberts & Gubbins (1987)). This diffusion contribution to SV modelling errors depends on the degree n and also on the decay-mode order, l, according to:

$$\Delta \dot{g}^{m,l}_{diff_n} = -(k^l_n)^2 \frac{\eta}{r_c^2} g^m_n \tag{8}$$

where $\eta = 5 \times 10^5$ Sm^{-1} is the core magnetic diffusivity and k_n^l is the l-th zero of the spherical Bessel function of order n. Supposing, as suggested by Holme & Olsen (2006), similar values for the radial and lateral length scales of the poloidal component of the MF, we represent in Figure 5 the estimate of diffusive effects based on the $l = n$ decay-modes.

4 Quasi-geostrophic modelling

In this section we outline the quasi-geostrophic approach on which we rely. It amounts to stating that the vorticity of the flow is predominantly axial and independent of the height z above the equatorial plane. Discussion of quasi-geostrophic modelling in deep spherical shells and reports of numerical simulations using this approximation - outside the tangent cylinder - can be found in e.g. Busse (1970), Cardin & Olson (1994), Aubert et al. (2003), Gillet & Jones (2006), Gillet et al. (2007).

The model considered for the Earth's core is that of a spherical shell container, rotating at angular velocity $\mathbf{\Omega} = \Omega\hat{\mathbf{z}}$. A cylindrical polar system of coordinates (s, ϕ, z) with the rotation axis as the polar axis is convenient to study rotation effects, where s is the distance to the axis, ϕ is the azimuthal angle and z is the height above the equatorial plane. The outer boundary corresponds to the core mantle interface, with shape defined by $z = H_c(s)$ and $z = -H_c(s)$ for the top and bottom boundary functions, where $H_c(s) = \sqrt{r_c^2 - s^2}$. In the same way, the inner boundary corresponds to the inner core surface, with shape defined by $z = \pm H_i(s)$, where $H_i(s) = \sqrt{r_i^2 - s^2}$ and r_i is the inner core radius. At the core surface, the rim of the TC is defined by the polar angle $\theta = \theta_0$, such that $r_i/r_c = \sin\theta_0$.

The two vectors normal to the top and the bottom external boundaries of the liquid core are, respectively,

$$\hat{\mathbf{r}}|_{\pm H_c} = \pm\hat{\mathbf{z}} - \frac{dH_c(s)}{ds}\hat{s} \qquad . \tag{9}$$

We note $\eta_c(s)$ the slope $|dH_c(s)/ds| = s/H_c$ of the outer boundary. A related parameter, widely used because of its equivalence to the latitudinal variation of the Coriolis parameter that enters the β-plane equations is

$$\beta(s) = \frac{\Omega\eta_c}{H_c} \qquad . \tag{10}$$

Likewise, we note $\eta_i(s)$ the slope $|dH_i(s)/ds| = s/H_i$ of the inner core boundary.

4.1 The classical expansion of the solution in powers of η_c

Let us first consider the region outside the tangent cylinder. We follow the discussion by Busse (1970) of instabilities in systems of slightly changing depths. Consider an expansion in powers of $\eta_c(s)$ for the velocity field. At the lowest order, the flow is assumed to be geostrophic,

$$2\rho\Omega\,\hat{\mathbf{z}} \times \mathbf{u}^0 = -\nabla p^0 \qquad , \tag{11}$$

where ρ is the fluid density, and obeys the Taylor-Proudman constraint $(\hat{\mathbf{z}} \cdot \nabla)\, \mathbf{u}^{\,0} = 0$. The solution (11) is completed by an expression for u_z^0,

$$u_z^0 = 0, \tag{12}$$

which corresponds to the no-penetration condition at the lowest order $\eta_c(s) = 0$, i.e., for constant depth. The solution of eq. (11) can be written, in cylindrical coordinates (s, ϕ, z):

$$\mathbf{u}^0(s,\phi) = -\hat{\mathbf{z}} \wedge \nabla\Psi(s,\phi) \Leftrightarrow \begin{cases} \quad u_s^0(s,\phi) = \frac{1}{s}\,\frac{\partial\Psi(s,\phi)}{\partial\phi} \\ \quad u_\phi^0(s,\phi) = -\frac{\partial\Psi(s,\phi)}{\partial s} \end{cases} \tag{13}$$

where $\Psi = -p^0/(2\rho\Omega)$ is the streamfunction describing the 0th-order flow. Taking into account the variation of H_c with s, the solution (11) does not satisfy the no-penetration condition $\mathbf{u}^0 \cdot \hat{\mathbf{r}} = \mathbf{0}$ at the boundaries. As a result, the term u_r^0 has to be added to the boundary condition for the flow at the next order.

The momentum equation, at the next order, gives us additional information on $\mathbf{u}^0$:

$$2\rho\Omega\,\hat{\mathbf{z}} \times \mathbf{u}^1 + \nabla p^1 = -\rho\frac{\partial \mathbf{u}^0}{\partial t} - \rho\mathbf{u}^0.\nabla\mathbf{u}^0 + \mathbf{j} \times \mathbf{B} \qquad . \tag{14}$$

Equation (14), where the viscous term is neglected, reflects our choice to emphasize a possible effect of the magnetic force on the core flow. We focus our attention on this term, and use (14) as a guide to derive regularization matrices for the flow inversion, because i) magnetic energy probably exceeds kinetic energy in the Earth's core ii) direct observations of the magnetic field changes point at the work of magnetic forces. Note that the importance of the buoyancy force, which is not included above, on the SV timescale is a very open question. Using the continuity equation $\nabla \cdot \mathbf{u}^1 = 0$, equation (14) can be readily transformed into an equation for the axial vorticity, where $\mathbf{u}^1$ enters only through $\partial u_z^1/\partial z$. Assuming that this latter term is z-independent, it can be derived from the boundary condition on $\mathbf{u}^1$. Using (9), the no-penetration boundary condition yields:

$$\mathbf{u} \cdot \hat{\mathbf{r}}|_{\pm H_c} = 0 \Leftrightarrow u_z^1|_{\pm H_c} = \mp\,\eta_c\,u_s^0(s,\phi)\ . \tag{15}$$

Finally, we obtain

$$u_z^1(s,\phi,z) = -\,\eta_c\,u_s^0(s,\phi)\,\frac{z}{H_c} = -\,\frac{sz}{H_c^2}\,u_s^0(s,\phi)\ . \tag{16}$$

From (14), (16) and (10), the vorticity equation averaged over the axial direction reduces to:

$$\frac{d\zeta}{dt} + 2\beta u_s^0 = \frac{1}{\rho}\,\frac{1}{2H_c}\int_{-H_c}^{H_c} \hat{\mathbf{z}} \cdot \nabla \wedge (\mathbf{j} \wedge \mathbf{B})\ dz \tag{17}$$

where ζ is the axial vorticity of the flow:

$$\zeta = -\nabla_E^2\Psi(s,\phi,t), \qquad \text{with} \qquad \nabla_E^2 = \frac{1}{s}\frac{\partial}{\partial s}\left(s\frac{\partial}{\partial s}\right) + \frac{1}{s^2}\frac{\partial^2}{\partial\phi^2} \tag{18}$$

The terms omitted assuming $\eta_c \ll 1$ have been shown to be not very important even when η_c is $O(1)$ in many instances (Jones , 2007). A necessary condition for the z-independent axial vorticity to dominate over other vorticity terms is

$$\eta_c \ll \frac{H_c}{l} \tag{19}$$

where l is a length scale in the equatorial plane. Finally, there is also a contribution to the stretching of vertical fluid lines, which is due to the pumping induced by mass conservation in the Ekman layer just below the CMB. This effect is negligible compared to the effect of impenetrable boundaries and it won't be considered here (see e.g. Schaeffer & Cardin (2005) for details or Olson et al. (2002) for a discussion in the context of core flow calculations).

4.2 The solution inside the tangent cylinder

It is well known (Heimpel et al., 2005) that the tangent cylinder corresponds to an important discontinuity for turbulent flows in rapidly rotating spherical shells. Some numerical studies show that convection may be organized differently respectively inside and outside the tangent cylinder (e.g., Sreenivasan & Jones (2006)). "Thermal" winds, possibly driven by composition gradients and modified by the magnetic field, may prevail within the tangent cylinder. On the other hand, it has been shown in a study of the motions spawned by an impulse of the solid inner core, that propagation of geostrophic shear inside the TC is also possible for Earth-like values of the parameter λ (see the Introduction) and of the Lundquist number, measuring magnetic dissipation (Jault, 2007).

Here, we consider, for want of anything better, that the main force balance there remains the same as outside the TC, and accordingly z-invariance of the equatorial flow in each hemisphere, separately, can still be foreseen.

Inside the tangent cylinder, fluid columns extend from the inner core to the outer core boundaries and must adjust to the two impenetrable surfaces. The two boundary conditions $\mathbf{u}\cdot\hat{\mathbf{r}}|_{r=r_c} = 0$ and $\mathbf{u}\cdot\hat{\mathbf{r}}|_{r=r_i} = 0$ give for the u_z^1 component inside the TC:

$$u_z^{1\pm}(s,\phi,z) = \eta_i u_s^{0\pm}\left[\frac{z \mp (H_i + H_c)}{H_c}\right] = \frac{s\,[z \mp (H_i + H_c)]}{H_i\,H_c}\, u_s^{0\pm}(s,\phi) \ , \tag{20}$$

where the plus and minus signs as superscripts in u_z^1 and u_s^0 refer to the northern and southern hemispheres, respectively. $u_s^{0\pm} = s^{-1}\partial\Psi^{\pm}(s,\phi)/\partial\phi$ is the northern and southern geostrophic radial component inside the TC. For a core interior point inside this region, both the external and the internal liquid core solid boundaries contribute to determine the axial flow and, near the TC, it's the inner core slope which is crucial. Note that equation (17) remains valid with β defined as:

$$\beta(s) = \frac{s\Omega}{H_i H_c} \qquad . \tag{21}$$

4.3 Application to the calculation of the flows inside the fluid outer core responsible for the observed secular variation

The neat expansion in powers of $\eta_c(s),\ \eta_i(s)$, outlined above, has to be modified in order to be coupled with equation (2). Indeed, this equation has been written using $\mathbf{u}\cdot\hat{\mathbf{r}} = 0$, which is not valid at the lowest order. Thus, it is necessary to add to the lowest order flow $\mathbf{u}^0$ some part of the first order flow $\mathbf{u}^1$.

The minimal modification consists in adding to $\mathbf{u}^0$ the term $u_z^1\,\hat{\mathbf{z}}$, with u_z^1 given by the expressions (16) and (20):

$$\mathbf{u}_{QG} = -\hat{\mathbf{z}}\wedge\nabla\Psi(s,\phi) + u_z^1(s,\phi,z)\,\hat{\mathbf{z}} \qquad . \tag{22}$$

Outside the TC, u_z^1 is of the order η_c and the whole flow depends on a single scalar streamfunction $\Psi(s,\phi)$. Inside the TC, u_z^1 is of the order η_i (the main slope effect) and two scalar functions $\Psi^+(s,\phi)$ and $\Psi^-(s,\phi)$ are required due to the decoupling of northern and southern hemispheres.

From equations (13) and (16), putting $s = r_c\sin\theta$, $z = \pm H_c$ and taking into account that $\partial/\partial s|_{r_c} = (r_c\cos\theta)^{-1}\partial/\partial\theta$ we can write for the trace of QG columns at the core surface, just below the Ekman layer and outside the TC:

$$\begin{aligned} u_\theta(\theta,\phi) &= \left(u_s^0\,\hat{\mathbf{s}} + u_z^1\,\hat{\mathbf{z}}\right)\cdot\hat{\theta} = \frac{1}{r_c\,\sin\theta\,\cos\theta}\,\frac{\partial}{\partial\phi}\Psi(\theta,\phi) \\ u_\phi(\theta,\phi) &= u_\phi^0 = -\frac{1}{r_c\,\cos\theta}\,\frac{\partial}{\partial\theta}\Psi(\theta,\phi) \qquad , \end{aligned}$$

which in condensed vectorial form yields

$$\mathbf{u}_H = -\frac{1}{\cos\theta}\hat{\mathbf{r}}\wedge\nabla_H\Psi(\theta,\phi) \qquad . \tag{23}$$

In the same way, from (13) with $\Psi^\pm$ instead of Ψ and from (20), the flow at the top of the core and inside the TC is:

$$\mathbf{u}_H^\pm = -\frac{1}{\cos\theta}\hat{\mathbf{r}}\wedge\nabla_H\Psi^\pm(\theta,\phi) \qquad . \tag{24}$$

The non-penetration condition on the velocity imposes that, at the intersection of the inner core and outer core boundaries with the Earth's equatorial plane, $u_s^0(s = r_i) = u_s^0(s = r_c) = 0$. From (13) this gives:

$$\begin{aligned} \Psi(s = r_i,\phi) &= \text{const.}\,, \\ \Psi(s = r_c,\phi) &= \text{const.}\,. \end{aligned} \tag{25}$$

It is readily apparent that the definition (22) of $\mathbf{u}_{QG}$ implies

$$\nabla_H\cdot(\mathbf{u}_{QG,H}\,\cos\theta) = 0, \tag{26}$$

at the core surface. This condition is well-known as describing a core surface flow which is compatible with a force balance dominated by the horizontal components of the Coriolis and pressure gradient forces as, for instance, the thermal wind balance. Such a flow, known as tangentially geostrophic, is also described in terms of a streamfunction linearly related to the pressure, just as in (23). Here, the above condition is much more restrictive since the underlying streamfunction Ψ is defined in the whole core and not only at the core surface. As a result of the z-invariance of Ψ, $\mathbf{u}_H$ must also be equatorially symmetric outside the TC. Acknowledging that the flow $\mathbf{u}_{QG}$ verifies at the core surface a condition widely used to invert geomagnetic models (tangentially geostrophic assumption) makes it easy to adapt already existing codes for our present purposes.

5 Specifying the regularization terms

5.1 Geometrical constraints directly derived from the physical model

The penalizing terms we use are consistent with the underlying dynamics. Accordingly, purely geometrical constraints typical of quasi-geostrophic vortices led to constrain the surface flow to be equatorially symmetric, not to cross the surface trace of the TC and to be tangentially geostrophic.

5.1.1 Tangential geostrophy

As discussed above, tangential geostrophy of the surface QG flow results from adopting the simplest modification of the leading order flow in order to meet the impermeability condition at the CMB and at the ICB. Yet, other choices could be made. For their definition of "columnar flows" Amit & Olson (2004) chose instead the first-order modification to the geostrophic flow $\mathbf{u}^0$ so that it is divergence-free. The difference between the two approaches is negligible if $\eta_c\, l/H_c \ll 1$, where l is the length scale of the flow in the equatorial plan (see Appendix A for a comparison between divergence-free and non divergence-free QG flows). Both Amit & Olson (2004) columnar flow and the quasi-geostrophy approaches are less well grounded for the largest scales of the core flow. It is thus fortunate that the QG approach blends at the core surface with the tangential geostrophy approach. Furthermore Gubbins (1991) and Jackson (1996) have shown that the radial vorticity equation at the core surface yields, under quite general hypotheses, a finite set of constraints that are obeyed by tangentially geostrophic flows.

In this study, the tangential geostrophy constraint is imposed as in Pais et al. (2004), by penalizing the integral $\int_{CMB} \left[\nabla_H \cdot (\mathbf{u}\cos\theta)\right]^2\, dS$ that can be written as $\mathbf{x}^T\mathbf{R}_G\mathbf{x}$. The penalizing factor that multiplies this term is made sufficiently high to guarantee that this condition is satisfied in practice all over the CMB.

5.1.2 Equatorial symmetry outside the rim of the tangent cylinder

Mirror symmetry of the core surface flow for reflection about the equatorial plane implies

$$\begin{aligned} u_\phi(\theta) &= u_\phi(\pi-\theta) \\ u_\theta(\theta) &= -u_\theta(\pi-\theta) \end{aligned} \qquad , \tag{27}$$

i.e., the azimuthal component is symmetric, whereas the latitudinal component is anti-symmetric. If equatorial symmetry was to be imposed over the whole CMB, the above conditions would require selection of only the $m+n$ even poloidal coefficients and only the $m+n$ odd toroidal coefficients. However, the special treatment of the volume inside TC leads to impose it only for $\theta > \theta_0$, where θ_0 is the colatitude of the rim of the tangent cylinder at the core surface. We then consider a grid of N_{grid} values of $\theta_0 < \theta < \pi/2$, where the following system of $2(2L_x+1)$ equations is to be satisfied:

$$
\begin{aligned}
&\sum_n 2\frac{dP_n^0}{d\theta}\left[1+(-1)^n\right] t_n^{0,c} = 0 \\
&\sum_{n\geq m} \frac{m}{\sin\theta} P_n^m \left[1-(-1)^{n+m}\right] s_n^{m,c(s)} \pm \sum_n \frac{dP_n^m}{d\theta}\left[1+(-1)^{n+m}\right] t_n^{m,s(c)} = 0, \quad m=1,...,L_x \\
&\sum_n 2\frac{dP_n^0}{d\theta}\left[1-(-1)^n\right] s_n^{0,c} = 0 \\
&\sum_{n\geq m} \frac{dP_n^m}{d\theta}\left[1-(-1)^{n+m}\right] s_n^{m,c(s)} \pm \sum_n \frac{m}{\sin\theta} P_n^m \left[1+(-1)^{n+m}\right] t_n^{m,s(c)} = 0, \quad m=1,...,L_x\ .
\end{aligned}
\tag{28}
$$

According to these equations, both $m+n$ odd poloidal and $m+n$ even toroidal coefficients may be present. Altogether, this gives a system of $2N_{grid}(2L_x+1)$ equations which, in matrix form, yields

$$
\mathbf{S}\,\mathbf{x} = \mathbf{0} \qquad ,
$$

where $\mathbf{S}$ is a $2N_{grid}(2L_x+1)\times 2L_x(L_x+2)$ matrix and $\mathbf{x}$ the vector of $2L_x(L_x+2)$ poloidal and toroidal coefficients of the flow. The related quadratic form in $\mathbf{x}$ that is penalized in the inversion is $\mathbf{x}^T\mathbf{R}_S\mathbf{x}$, where $\mathbf{R}_S = \mathbf{S}^T\mathbf{S}$.

5.1.3 Zero latitudinal flow on the rim of the tangent cylinder

As already pointed out, the impermeability condition on the inner core surface requiring that $u_s^0 = 0$ at $s = r_i$, implies that $u_\theta = 0$ at the CMB, on the rim of the TC, i.e.,

$$
\begin{aligned}
u_\theta(\theta_0,\phi) &= 0 \\
u_\theta(\pi-\theta_0,\phi) &= 0 \qquad .
\end{aligned}
\tag{29}
$$

This yields the following system of $2L_x+1$ equations to be verified for $\theta=\theta_0$ and $\theta = \pi-\theta_0$,

$$
\begin{aligned}
&\sum_n \frac{1}{2}\frac{dP_n^0}{d\theta} s_n^{0,c} = 0 \\
&\sum_n \frac{dP_n^m}{d\theta} s_n^{m,c(s)} \pm \sum_n \frac{m}{\sin\theta} P_n^m\, t_n^{m,s(c)} = 0 \qquad m=1,...,L_x \qquad ,
\end{aligned}
\tag{30}
$$

and that can be written, in matrix form,

$$\mathbf{T}\,\mathbf{x} = \mathbf{0} \qquad .$$

The first relation in (30) is trivially satisfied by tangentially geostrophic flows. $\mathbf{T}$ is a $2(2L_x+1) \times 2L_x(L_x+2)$ matrix. The quadratic form to be penalized in the inversion is $\mathbf{x}^T \mathbf{R}_T \mathbf{x}$, where $\mathbf{R}_T = \mathbf{T}^T \mathbf{T}$.

5.2 Constraints used as proxies of a comprehensive dynamical model

Having simplified the vorticity equation into the equation (17) for axial vorticity, it should eventually be possible to estimate core flows that both account for SV observations and evolve in response to magnetic and rotation forces. In the meantime, we consider this study as an intermediate step. Many authors (Galperin et al., 2001; Danilov & Gurarie, 2002) have already considered quasi-geostrophic turbulence without the presence of a magnetic field. They have observed that because of the β-term (second term on the LHS of equation (17)), a zonation effect occurs whereby latitudinal flows are penalized and large scale motions are predominantly in the ϕ-direction. We mimic this effect in our inversion by penalizing radial motions u_s multiplied by the weight β. We have not much information on magnetic forces acting on the fluid. Yet, we do know that they are the counterpart of induction of magnetic field. We can thus assume that magnetic forces tend to oppose motions able to produce magnetic fields. We tentatively account for this effect by penalizing horizontal gradients in the QG velocity field. Finally, we also minimize the kinetic energy integrated in the fluid outer core. The following three regularization terms can be written as quadratic forms in the CMB flow coefficients, as explained in Appendix B.

5.2.1 Minimization of the β-effect

The term βu_s enters the equation for axial vorticity defined in the equatorial plane. We penalize the surface integral of $|\beta u_s|^2$ over the equatorial section. From equations (13), (10) and (21) this amounts to penalize the following integral, on the CMB,

$$\int_0^{2\pi} \left(\int_0^{\theta_0} + \int_{\pi-\theta_0}^{\pi}\right) \left(\frac{1}{H_c H_i}\frac{\partial}{\partial\phi}\Psi\right)^2_{CMB} |\cos\theta| \sin\theta\, d\theta\, d\phi$$
$$+ \int_0^{2\pi} \int_{\theta_0}^{\pi-\theta_0} \left(\frac{1}{H_c^2}\frac{\partial}{\partial\phi}\Psi\right)^2_{CMB} |\cos\theta| \sin\theta\, d\theta\, d\phi \qquad , \tag{31}$$

where the factor $\cos\theta$ is for the projection of the surface element on the equatorial section and no distinction is made between the core surface streamfunction inside and outside the rim of the TC, as one same set of spherical harmonic coefficients is used to characterize it. Using Appendix B, it can be readily noticed that penalizing βu_s inside the core amounts to penalize certain relations between the poloidal coefficients that characterize the surface flow. We have computed the elements of the matrix $\mathbf{R}_\beta$ that make possible to write (31) as a quadratic form on $\mathbf{x}$, $\mathbf{x}^T \mathbf{R}_\beta \mathbf{x}$.

5.2.2 Minimization of the rate of strain tensor elements

Magnetic field induction yields the time changes of magnetic energy, $\int_V B_i B_j e_{ij}\, dV$, where $e_{ij} = 1/2\,(\partial u_i/\partial x_j + \partial u_j/\partial x_i)$ is the rate of strain tensor in Cartesian coordinates $x_i, (i = 1, 2, 3)$ (see e.g. Fearn et al. (1988)). For QG flows, the flow deformation is mainly two-dimensional, in the plane perpendicular to the rotation axis.

The plane symmetric tensor $\mathbf{e}$ has only two independent elements, since the non-divergence of the equatorial leading order flow carries the further condition that its trace must be zero. Then, in cylindrical coordinates,

$$
\begin{aligned}
e_{s\,\phi} = e_{\phi\,s} &= \frac{1}{2}\left(\frac{1}{s^2}\frac{\partial^2\Psi}{\partial\phi^2} - \frac{1}{s}\frac{\partial\Psi}{\partial s} + \frac{\partial^2\Psi}{\partial s^2}\right) \\
e_{s\,s} = -e_{\phi\,\phi} &= -\frac{1}{s^2}\frac{\partial\Psi}{\partial\phi} + \frac{1}{s}\frac{\partial^2\Psi}{\partial s\partial\phi} \qquad .
\end{aligned} \tag{32}
$$

As none of the terms in (32) is z-dependent, each integration over the equatorial plane section can transform into an integration over the core surface, as in the preceding section, where the contribution of the two, North and South hemispheres, is contemplated. Using the description of the core surface Ψ in terms of poloidal and zonal toroidal CMB flow coefficients, as given in eq. (44), we sum the two independent integrals to derive a new quadratic form in $\mathbf{x}$, $\mathbf{x}^T\mathbf{R}_e^{-1}\mathbf{x}$.

5.2.3 Energy minimization

The penalization of the surface kinetic energy density, has been used as a weak regularization for CMB flow inversions (e.g. Pais et al. (2004)), as one possible way to regularize the flows while avoiding to restrict too strongly medium to small flow scales. Here, having a model for the whole core flow, we can derive expressions for the whole flow kinetic energy density $\int_V \mathbf{u}\cdot\mathbf{u}dV = \int_V (u_\phi^{0^2} + u_s^{0^2} + u_z^{1^2})dV$, where V denotes the liquid core volume. These three contributions can be expressed in terms of the streamfunction Ψ at the core surface, according to the following three relations:

$$
\int_V u_s^{0^2}\, dV = r_c \int_0^{2\pi}\int_0^{\pi}\left(\frac{\cos\theta}{\sin\theta}\frac{\partial}{\partial\phi}\Psi\right)^2_{CMB} \sin\theta\, d\theta\, d\phi \qquad , \tag{33}
$$

$$
\int_V u_\phi^{0^2}\, dV = r_c \int_0^{2\pi}\int_0^{\pi}\left(\frac{\partial}{\partial\theta}\Psi\right)^2_{CMB} \sin\theta\, d\theta\, d\phi \qquad , \tag{34}
$$

$$
\begin{aligned}
\int_V u_z^{1^2}\, dV = \frac{r_c^2}{3}\int_0^{2\pi}\left(\int_0^{\theta_0} + \int_{\pi-\theta_0}^{\pi}\right)\left[\frac{H_c^3 - H_i^3}{H_c^2 H_i^2}\left(\frac{\partial}{\partial\phi}\Psi\right)^2\right]_{CMB} |\cos\theta|\sin\theta\, d\theta\, d\phi \\
+ \frac{r_c}{3}\int_0^{2\pi}\int_{\theta_0}^{\pi-\theta_0}\left(\frac{\partial}{\partial\phi}\Psi\right)^2_{CMB}\sin\theta\, d\theta\, d\phi \qquad .
\end{aligned} \tag{35}
$$

Notice that no distinction is made between the three streamfunction Ψ, Ψ^+ and Ψ^- at the core surface, because they are described there in terms of the same set of spherical harmonic coefficients (see Appendix B). The sum of the previous three terms is written as $\mathbf{x}^T\mathbf{R}_E^{-1}\mathbf{x}$, and establishes the third quadratic form to be penalized.

6 Results

The iterative procedure increases by 10 to 15 times (the number of steps needed for convergence) the time allocated to each flow computation. In addition, the number of regularizing norms used to tune the flow inversion sets up the dimension of the domain of parameters $(\lambda_\beta, \lambda_e, \lambda_E)$. Because of the high number of computations required, we did not explore the domain of parameters in a systematic way, as in Pais et al. (2004). Instead, following a trial and error approach, we have set $(\lambda_\beta = 1.0 \times 10^6, \lambda_E = 1.0 \times 10^5)$ and we determine two values of the parameter λ_e so that the normalized error $\chi \sim 1.0$ for the final converged flows $\hat{\mathbf{x}}_1$ and $\hat{\mathbf{x}}_2$.

Flows computed using either the 'pessimistic' or the 'optimistic' initial errors for the SV model, are characterized in Tables 1 and 2 for epoch 2001.0. In addition to standard quantities as the core surface RMS (root mean square) flow speed, $v^{(S)}_{RMS} = \left(\int_{CMB} \mathbf{u} \cdot \mathbf{u}\, dS/4\pi r_c^2\right)^{1/2}$, we can also compute other physical quantities characterizing the interior flow. It is the case of the RMS βu_s term over the equatorial plane, $\beta_{effect} \sim \Omega\sqrt{\mathbf{x}^T \mathbf{R}_\beta \mathbf{x}}$, the RMS volume energy, $v^{(V)}_{RMS} \sim \sqrt{\mathbf{x}^T \mathbf{R}_E \mathbf{x}}$, and the RMS strain tensor elements over the equatorial plane, $e_{effect} \sim \sqrt{\mathbf{x}^T \mathbf{R}_e \mathbf{x}}$, which we show in those tables. Besides, values of $\sqrt{\mathbf{x}^T \mathbf{R}_G \mathbf{x}}$, $\sqrt{\mathbf{x}^T \mathbf{R}_S \mathbf{x}}$ and $\sqrt{\mathbf{x}^T \mathbf{R}_T \mathbf{x}}$ can be used to appraise how close the geometrical constraints are satisfied by the flow. We obtain, for all computed flows, values of the order 10^{-6} for the latter three quantities (see section 5.1), in units of km/yr. These values, which serve to quantify the velocity components violating the geometrical constraints, are much smaller than $v^{(S)}_{RMS}$ or $v^{(V)}_{RMS}$.

We note that the RMS velocity is higher at the surface than in the volume. Indeed, the flow energy density, proportional to $u^2(s, \phi, z)$, always increases with z from the equatorial plane to the CMB since u_s and u_ϕ are z-invariant while u_z^2 increases, outside TC, as z^2.

To clarify the description and discussion of results, let us set the interval $n \lesssim 6$ as defining *large scales*, $6 \lesssim n \lesssim 13$ for *intermediate scales* and $n \gtrsim 13$ for *small scales*.

In Figures 6 and 7 we show results characterizing the iterative inversion for epoch 2001.0, using the regularization terms specific of this study. Neither the power spectra of the SV misfit at the Earth's surface (Fig. 6), nor charts of global distribution of SV misfit (not shown) indicate any significant spatially localized features. We do not find any particular region where equatorial symmetry or zero latitudinal flow on the rim of the TC are harder to verify. Two cases, when using 'pessimistic' or 'optimistic' initial errors, are analyzed. Comparison with Figure 3 shows a somewhat higher modelling error, due to an overall weaker regularization. Figure 6 further confirms similar values obtained for the difference between the SV produced by advection of BL by flows 1 and 2, on the one hand, and the SV due to advection of BS by flow 2, on the other hand. We also show the estimate of diffusive effects based on $l = n$ decay-modes (Holme & Olsen, 2006). It clearly stands out that the modelling error associated to under-parameterization of the MF is more important than the magnetic diffusion modelling error computed in this way. This is globally true over all length scales, and particularly for the largest ones. We should note, however, that if we treat the dipole separately, as often done due to its relatively huge size, and consider a decay mode of order greater than one, its contribution increases to levels of the same order of magnitude as the hidden MF error (see also Holme & Olsen (2006)).

Comparing the left and right columns of Figure 6, it stands out that the improvement brought to explanation of intermediate scales of SV by initial small errors, does deteriorate the fit quality to SV large scales. This is due to smaller flow scales that are required (see Figure 7), in the interval $n \sim 15-18$, which also contribute to large scale SV by advecting BS. We also show in Figure 7, the curve of mean energy per degree corresponding to an energy spectrum depending on n^{-2}. Only for degrees above ~ 15, using 'pessimistic' initial errors, or above $\sim$ 18, when using 'optimistic' initial errors, do the computed values converge. For those smaller scales, where convergence is steeper than for a n^{-2} spectrum, the statistical flow assumptions of Hulot et al. (1992) leading to their estimate of the SV signal that results from the interaction between BS and the flow (see section 3.1) apply, but not before.

Figures 8 and 9 show the maps of axial vorticity in an equatorial section for the three epochs 2001.0, 2002.5, and 2004.0, when using 'pessimistic' and 'optimistic' initial errors, respectively. An orthographic projection is used, which has the particular advantage that, if the central point is one of the poles, the corresponding hemisphere is projected onto the equatorial plane. In case of z-invariance, this 2D representation gives all the information on the flow. Common to the two sets of charts, is the clustering of vortices around the rim of the TC, especially over the hemisphere west to the Greenwhich meridian. The Ψ streamfunction maps shown in Figure 10 unambiguously outline these vortices.

The Ψ maps are useful to describe the largest scales of the flow. The most noticeable feature is a grand westward jet circling round the inner core. It touches the inner core from around 135^{o}W to 150^{o}E, and moves to larger radii in the Atlantic hemisphere, in a band 30^o away from the equator, from around 90^{o}E to 90^{o}W. The main lines of this feature have been noticed before, in flows inverted using the spectral method with the toroidal, steady or tangentially geostrophic flow assumptions (see e.g. Bloxham (1991)). Recently, it has been seen in the relatively fine-scale core surface flows of Holme & Olsen (2006) and also in the time average flow for 1840-1990 obtained by Amit & Olson (2006) using a grid-based finite difference method. The equatorial symmetry of this flow, imposed in the present work, is not always clear in previous studies, where often the low latitude jet is more pronounced in the Southern than in the Northern hemispheres. When an important equatorial symmetry was noticed, this feature has been related to cylindrical rotation about an axis parallel to the Earth's rotation axis (e.g. Bloxham (1991)). Also, in some previous studies, the high latitude jet crosses the rim of the TC and closes into a complete large vortex centered beneath the Southern Atlantic Ocean (e.g. Amit & Olson (2006)). Here, where crossing over high latitudes is impeded, the large jet closes by encircling the inner core. Accordingly, the single large jet feature not only incorporates the well-known low latitude westward drift, beneath the Indian and Atlantic oceans, but also a less frequently reported high latitude westward drift beneath the Bering Sea. The often reported anti-cyclonic vortex centered beneath North America (e.g. Amit & Olson (2006)) merges with the also reported anti-cyclonic vortex beneath the Arabian Peninsula (e.g. Bloxham (1989)) to give the northern hemisphere counterpart of this large scale feature. Equatorial symmetry inside the rim of the TC being not imposed, we also recover another known result, namely a polar vortex more conspicuous in the Northern than in the

Southern hemispheres (e.g. (Olson et al., 1999)), except for epoch 2004.0 (see Figure (11)). Eventually, it is possible that inverting for separate streamfunctions inside and outside the TC, will better resolve the asymmetry inside TC.

Smaller scale vortices, of diameter ∼700km ($m \sim 6$), cluster around the rim of TC. Particularly robust to the change in SV model error criteria (compare Figures 8 and 9), are the cyclonic features between 135 and 225^{o}E, and the two anti-cyclonic vortices centered at $\sim 45^o$W and $\sim 120^o$W. Between the two of them, a cyclonic vortex centered at $\sim 90^o$W seems also to be present. One other cyclonic/anti-cyclonic pair can be identified between 90^{o}E and 120^{o}E, in all charts except for 2004.0. The localization of these main features being very stable all over the 3-years time span considered, the associated vorticity intensity does apparently change, though we can not say how robust is this result.

We have wondered how crucial is each constraint used as proxy of a dynamical effect. We have thus calculated flows using only one constraint ($\lambda_\beta = \lambda_e = 0$ or $\lambda_\beta = \lambda_E = 0$ or $\lambda_e = \lambda_E = 0$) at a time. We have found that the large jet structure is present in these three extreme cases. Well defined vortices clustered around the TC appear, centered at similar positions, when minimizing either the βu_s term - which promotes vortices more elongated along parallels - or the strain tensor elements. From a closer look at these results we can advance that the flows we present in this study are dominantly constrained by the minimization of the rate of strain tensor elements. The other two regularizations do, nonetheless, introduce additional physically motivated constraints on the flow coefficients, which contribute to decrease the number of free parameters in the inversion.

Of particular geophysical interest, is the time variation of the zonal component of our computed flows, since it can be related to geodetic observations of the Earth's rotation. The zonal component of the QG flow consists in the cylindrical annuli responsible for changes in the axial angular momentum of the liquid core. We can then compute

$$L_z = \rho \int_V s u^0_\phi(\theta)\, dV \tag{36}$$

(Jault et al, 1988; Jackson et al, 1993) and compare $L_z(t)$, from our computed flows, with $(I_c + I_m)(2\pi/T_0^2)\Delta LOD(t)$ from geodetic observations, where I_c and I_m are the moments of inertia of the core and mantle, respectively, and T_0 is the reference value for the length-of-day (LOD). This is done in Figure 12, where, as observations, we use annual means of LOD, computed from the IERS CO4 series of daily values. No matter the initial SV error used, the change of tendency at the middle epoch is always recovered.

It is customary to simplify the computation of (36) by neglecting the inner core volume and approximating the fluid core to a spherical liquid-filled cavity. This is of course supported, on the basis of the very small moment of inertia of the centered liquid sphere having the inner core radius. Considering, separately, the fluid region inside TC, Jackson (1997) further confirmed that its contribution to the total angular momentum is much smaller than that of the region outside the TC. This result still applies for our computed flows. However, we also find that, from one epoch to the other, the amount of angular momentum variation of the inside region can be of the same order of magnitude as that of the outside region. We also computed $L_z(s') =$

$\rho \int_0^{s'} s u_\phi^0 \, dV$, the axial angular momentum contribution of the liquid core with $s < s'$. We then confirm the minor contribution of the region inside the TC ($s < r_i$). However, showing the curve $T_0^2/[2\pi(I_c + I_m)] \, dL_z(\theta)/d\theta$ (i.e. the core contribution, per degree of latitude, to LOD variation) in Figure 13, we make apparent that the core angular momentum is concentrated in two latitudinal bands, the first one between 20^o and 30^o colatitude, and the second one at almost 60^o colatitude. Crossing this information with the streamfunction charts, we realize that the axial angular momentum of the core is mainly carried by the large jet feature identified above.

7 Discussion and Conclusions

Several interesting conclusions can be drawn from the flow inversions described above. First, we find that intermediate scales ($n \sim 6 - 13$) of the SV, made known by recent magnetic satellite missions, have a significant contribution from advection of the magnetic field by intermediate to small scale flows. These results show that the limitation brought by using truncated series at a relatively low degree, say 13, of the flow scalar potentials, which would not be a critical issue if the flow was large-scale, with an energy spectrum converging below the truncation spherical harmonic degree, is presently hampering the identification of flows responsible for the finest SV structures recently resolved. In fact, no strong physical argument exists to support a large scale assumption on the decade timescale, much on the contrary.

Second, we are able to estimate part of the modelling error that results from the ignorance of the core magnetic field with harmonic degree $n \geq 14$. We concur with Eymin & Hulot (2005) in noting that, as it happens, this modelling error is much more important than the observational errors, for SV low harmonic degrees. As a result, it is much more critical to have an accurate knowledge of the observational errors for scales of the SV corresponding to $n \gtrsim 8$ - as exemplified by a comparison between calculations (Figures 8 and 9) made with respectively 'pessimistic' and 'optimistic' estimates for the errors - than for the large scales. We use our estimate of the modelling error to correct iteratively for the covariance matrix $\mathbf{C_y}$, and to invert for more consistent flows. Of course, we can anticipate that further increasing the space resolution of SV, will worsen even more the fit to large scale SV. Eventually, the paradigm of a large scale SV due to advection of the field by a large scale flow may have to be revised.

Third, we suggest new geometrical constraints on the flow. We find that it is possible to account for the secular variation models derived from satellites data with motions symmetrical with respect to the equator outside the tangent cylinder that can be continued inside the core as quasi-geostrophic motions. We are thus able to present maps of axial vorticity in the equatorial plane. We resolve vortices of azimuthal harmonic degree $m \sim 6$ and diameter ~ 700 km just outside TC.

Finally, we recover the often commented asymmetry between the Atlantic and Pacific Hemispheres that is characteristic of secular variation models for recent epochs. Strong anticyclones in the Atlantic hemisphere contrast with weak cyclones in the Pacific hemisphere. We notice a westward jet, also asymmetric, circling around the inner core, that moves closer to TC in the Pacific hemisphere. Its geometry results from the constraint that flows cannot cross TC. It carries most of the core angular momentum.

We find a satisfactory agreement between our estimates for core angular momentum changes and estimates derived from LOD observations using conservation of the total Earth angular momentum.

We note that the contribution of the fluid region inside the tangent cylinder to the total angular momentum is very small, between 4 and 9 percent and 6 and 8 percent with 'optimistic' and 'pessimistic' estimates for the SV error, respectively. However, its contribution to the time changes of core angular momentum is important enough. Indeed, the related estimate of excess length-of-day due to this fraction alone of the core is of the order of 10^{-4} s. This observation may point to a role of the solid inner core in the mechanism responsible for interannual changes in core angular momentum (see e.g. Mound & Buffett (2003)).

What confidence can we have in these velocity maps? Quasi-geostrophy requires that the height $H_c(s)$ do not vary too rapidly with the distance s to the rotation axis. Thus, this approximation may not work well near the outer rim of the equatorial section, which corresponds to the low latitudes at the core surface. This is the very region where the tests of core flow imaging methods with numerical dynamos conducted by Rau et al. (2000) and Amit et al. (2007) fail. These authors have attributed the poor recovery of surface flows there to radial magnetic diffusion. By penalizing βu_s, we ensure that our axial vorticity maps are, at least, consistent with the QG hypothesis on which we rely. Hopefully, some spurious flows in the equatorial region are also avoided.

The present study can be viewed either as an alternative or as a complement to recent investigations of core surface flows controlled by lateral variations in the heat flux at the CMB (Lister, 2004; Amit & Olson, 2006; Aubert et al., 2007). We have noticed that several small-scale vortices of fluctuating intensity are required to account for the satellite data. These can hardly be controlled by thermal features standing in the lower mantle for millions of years. On the other hand, the QG approach is the least grounded for the largest scales of the flow that cannot be inferred from the z-averaged axial vorticity alone. Aubert (2005) and Aubert et al. (2007) have recently argued, on the basis of numerical simulations of dynamos driven either by homogeneous or by heterogeneous boundary heat flux, that a thermal wind balance holds for steady flows. At the core surface, thermal winds are tangentially geostrophic. Thus, an interesting development of the present study is to try to account for the secular variation with core flows of which the rapidly varying small scale components are QG and the large scale components are either unconstrained or tangentially geostrophic.

We consider the present work as a step towards a fully dynamical study of core flows. We have shown that QG flows may account for geomagnetic SV. We can now contemplate adding to the information provided by SV models the equation (17) that governs the evolution of QG core flows, applying the geomagnetic data assimilation method outlined by Fournier et al. (2007) with a more realistic physical model.

Our study relies on a SV model derived from satellite data that resolves much smaller length scales than the historical models of the magnetic field that were used in core flow modelling until a few years ago. We are well aware, however, that such a model remains preliminary and that further improvements can be expected in the years to come. Models incorporating dynamical constraints like the model presented here will be required to fully benefit from these efforts in recording and modelling the Earth's magnetic field.

Acknowledgments

The first version of the paper benefited from the careful reading of Alexandre Fournier and Henri-Claude Nataf. Comments of the paper editor, R. Holme, Hagay Amit and an anonymous referee have been very useful to revise the initial manuscript. This work has been initiated during the stay of AP as CNRS associate in LGIT. It has been supported by a grant from the French Agence Nationale de la Recherche, Research program VS-QG (grant number BLAN06-2.155316) and by the Cooperation Program PESSOA, between the Portuguese and the French scientific agencies GRICES / ÉGIDE.

References

Amit, H., and P. Olson, 2004. Helical core flow from geomagnetic secular variation. *Phys. Earth Planet. Int.*, **147**, doi:10.1016/j.pepi.2004.02.006, 1–25.

Amit, H., and P. Olson, 2006. Time-average and time-dependent parts of core flow. *Phys. Earth Planet. Int.*, **155**, doi:10.1016/j.pepi.2005.10.006, 120–139.

Amit, H., P. Olson and U. Christensen, 2007. Tests of core flow imaging methods with numerical dynamos. *Geophys. J. Int.***168**, 27–39.

Aubert, J., 2005. Steady zonal flows in spherical shell dynamos. *J. Fluid Mech.*, **542**, 53–67.

Aubert, J., D. Brito, H.-C. Nataf, P. Cardin and J.-P. Masson 2001. A systematic experimental study of rapidly rotating spherical convection in water and liquid gallium. *Phys. Earth Planet. Int.*, **128**, 51–74.

Aubert, J., N. Gillet and P. Cardin 2003. Quasigeostrophic models of convection in rotating spherical shells. *G3*, **4**, 1052, doi:10.1029/2002GC000456.

Aubert, J., H. Amit and G. Hulot, 2007. Detecting thermal boundary control in surface flows from numerical dynamos. *Phys. Earth Planet. Int.*, **160**, doi:10.1016/j.pepi.2006.11.003, 143–156.

Backus, G.E., 1968. Kinematics of geomagnetic secular variation in a perfectly conducting core, *Phil. Trans. Soc. Lond. A*, **263**, 239–266.

Bloxham, J., 1988. The dynamical regime of fluid flow at the core surface, *Geophys. Res. Lett.*, **15**, 585–588.

Bloxham, J., 1989. Simple models of fluid flow at the core surface derived from geomagnetic field models, *Geophys. J. Int.*, **99**, 173–182.

Bloxham, J., A. Jackson. 1991. Fluid flow near the surface of Earth's outer core, *Rev. Geophys.*, **29**, 97–120.

Busse, F.H., 1970. Thermal instabilities in rapidly rotating systems. *J. Fluid Mech.*, **44**, 441–460.

Busse, F.H., 1976. Generation of planetary magnetism by convection. *Phys. Earth Planet. Int.*, **12**, 350–358.

Busse, F.H., 2002. Convective flows in rapidly rotating spheres and their dynamo action. *Phys. Fluids*, **14**, 1301–1314.

Cardin, P. and P. Olson, 1994. Chaotic thermal convection in a rapidly rotating spherical shell: consequences for flow in the outer core. *Phys. Earth Planet. Int.*, **82**, 235–259.

Celaya, M., and J. Wahr, 1996. Aliasing and noise in core-surface flow inversions. *Geophys. J. Int.*, **126**, 447–469.

Christensen, U. and J. Aubert, 2006. Scaling properties of convection-driven dynamos in spherical rotating shells and application to planetary magnetic fields. *Geophys. J. Int.*, **166**, 97–114.

Chulliat, A., and G. Hulot, 2000. Local computation of the geostrophic pressure at the top of the core. *Phys. Earth Planet. Int.*, **117**, 309–328.

Danilov, S., and D. Gurarie, 2002. Rhines scale and spectra of the β-plane turbulence with bottom drag. *Physical Review E*, **65**, doi:10.1103/PhysRevE.65.067301, 067301.

Eymin, C., and G. Hulot, 2005. On core surface flows inferred from satellite magnetic data. *Phys. Earth Planet. Int.*, **152**, doi:10.1016/j.pepi.2005.06.009, 200–220.

Fearn, D., P.H. Roberts and A.M. Soward, 1998. Convection, stability and the dynamo, in *Energy stability and convection*, G.P. Galdi & B. Straughan, editors, Longman Scientific and Technical, Harlow.

Fournier, A., C. Eymin and T. Alboussiere, 2007. A case for variational geomagnetic data assimilation: insights from a one-dimensional, nonlinear, and sparsely observed MHD system. *Nonlinear processes in geophysics*, **14**, 163-180.

Galperin, B., S. Sukoriansky and H.-P. Huang, 2001. Universal n^{-5} spectrum of zonal flows on giant planets. *Phys. Fluids*, **13**, 1545-1548.

Gillet, N., and C.A. Jones, 2006. The quasi-geostrophic model for rapidly rotating spherical convection outside the tangent cylinder. *J. Fluid Mech.*, **554**, 343–369.

Gillet, N., D. Brito, D. Jault and H.-C. Nataf., 2007. Experimental and numerical studies of convection in a rapidly rotating spherical shell. *J. Fluid Mech.*, **580**, 83–121.

Gire, C., and J. L. Le Mouël, 1990. Tangentially geostrophic flow at the core-mantle boundary compatible with the observed geomagnetic secular variation: the large-scale component of the flow. *Phys. Earth Planet. Int.*, **59**, 259–287.

Glatzmaier, G. and P.H. Roberts, 1995. A three-dimensional self-consistent computer simulation of a geomagnetic field reversal. *Nature*, **377**, 203–209.

Gubbins, D., 1991. Dynamics of the secular variation. *Phys. Earth Planet. Int.*, **68**, 170–182.

Gubbins D. and P.H. Roberts, 1987. Magnetohydrodynamics of the Earth's core, in *Geomagnetism, volume 2*, J.A. Jacobs, editor, Academic Press, London.

Heimpel, M., J. Aurnou and J. Wicht, 2005. Simulation of equatorial and high-latitude jets on Jupiter in a deep convection model. *Nature*, **438**, 193–196.

Holme, R., and N. Olsen, 2006. Core surface flow modelling from high-resolution secular variation. *Geophys. J. Int.*, **166**, doi:10.1111/j.1365-246X.2006.03033.x, 518–528.

Hulot, G., J. L. Le Mouël and D. Jault, 1990. The flow at the core-mantle boundary: symmetry properties, *J. Geomag. Geoelectr.*, **42**, 857–874.

Hulot, G., J. L. Le Mouël and J. Wahr, 1992. Taking into account truncation problems and geomagnetic model accuracy in assessing computed flows at the core-mantle boundary, *Geophys. J. Int.*, **108**, 224–246.

Hulot, G., C. Eymin, B. Langlais, M. Mandea and N. Olsen, 2002. Small-scale structure of the geodynamo inferred from Oersted and Magsat satellite data, *Nature*, **416**, 620–623.

Jackson, A., 1996. Kelvin's theorem applied to the Earth's core, *Proc. R. Soc. Lond. A*, **452**, 2195-2201.

Jackson, A., 1997. Time-dependency of tangentially geostrophic core motions, *Phys. Earth Planet. Int.*, **103**, 293-311.

Jackson, A., J. Bloxham and D. Gubbins, 1993. Time-dependent flow at the core surface and conservation of angular momentum in the coupled core-mantle system, *Dynamics of the Earth's deep interior and Earth rotation*, Eds J.L. Le Mouël, D.E. Smylie and T. Herring, Geophysical Monograph Series **92**, 97-107.

Jault, D., submitted. Axial invariance of rapidly varying diffusionless motions in the Earth's core interior. *Phys. Earth Planet. Int.*.

Jault, D., C. Gire and J.-L. Le Mouël, 1988. Westward drift, core motions and exchanges of angular momentum between core and mantle. *Nature*, **333**, 353-356.

Jones C.A., 2007. Thermal and compositional convection in the outer core, in *Treatise on Geophysics, Volume 8 Core dynamics*, G. Schubert, editor, Elsevier.

Jones C.A., A.I. Mussa and S.J. Worland, 2003. Magnetoconvection in a rapidly rotating sphere: the weak-field case. *Proc. Roc. Soc.*A, **459**, 773–797.

Langel, R.A. and R.H. Estes, 1982. A geomagnetic field spectrum, *Geophys. Res. Lett.*, **9**, 250–253.

Le Huy, M., M. Mandea, J.-L. Le Mouël, A. Pais, 2000. Time evolution of the fluid flow at the top of the core. *Earth Planets Space*, **52**, 163–173.

Le Mouël, J.-L., C. Gire and T. Madden, 1985. Motions at the core surface in geostrophic approximation. *Phys. Earth Planet. Int.*, **39**, 270–287.

Lister, J.R., 2004. Thermal winds forced by inhomogeneous boundary conditions in rotating, stratified hydromagnetic fluid. *J. Fluid Mech.*, **505**, 163–178.

Maus, S., M. Rother, C. Stolle, W. Mai, S. Choi, H. Lühr, D. Cooke and C. Roth, 2006. Third generation of the Potsdam Magnetic Model of the Earth (POMME). *Geochem. Geophys. Geosyst.*, **7**, doi:10.1029/2006GC001269.

Mound, J. E. and B. A. Buffett, 2003. Interannual oscillations in length of day: Implications for the structure of the mantle and core, *J. geophys. Res.***108**, doi:10.1029/2002JB002054.

Olsen, N. and M. Mandea, 2007. Investigation of a secular variation impulse using satellite data: The 2003 geomagnetic jerk. *Earth planet. Sci. Lett.***255**, 94–105.

Olsen, N., H. Lühr, T.J. Sabaka, M. Mandea, M. Rother, L. Tøffner-Clausen and S. Choi, 2006 CHAOS - a model of the Earth's magnetic field derived from CHAMP, Ørsted, and SAC-C magnetic satellite data. *Geophys. J. Int.***166**, 67–75.

Olson, P. and J. Aurnou, 1999. A polar vortex in the Earth's core. *Nature*, **402**, 170–173.

Olson, P., U. Christensen and G.A. Glatzmaier, 1999. Numerical modeling of the geodynamo: mechanisms of field generation and equilibration. *J. geophys. Res.***104**, 10383–10404.

Olson, P., I. Sumita and J. Aurnou, 2002. Diffusive magnetic images of upwelling patterns in the core. *J. geophys. Res.***107**, doi:10.1029/2001JB000384.

Pais, A., and G. Hulot, 2000. Length of day decade variations, torsional oscillations and inner core superrotation: evidence from recovered core surface zonal flows. *Phys. Earth Planet. Int.*, **118**, 291–316.

Pais, M. A., Oliveira, O. and F. Nogueira, 2004. Nonuniqueness of inverted core-mantle boundary flows and deviations from tangential geostrophy, *J. geophys. Res.***109**, doi:10.1029/2004JB003012.

Rau, S., U. Christensen, A. Jackson and J. Wicht, 2000. Core flow inversion tested with numerical dynamo models, *Geophys. J. Int.*, **141**, 485–497.

Roberts, P.H. and D. Gubbins, 1987. Origin of the main field: kinematics, in *Geomagnetism, volume 2*, J.A. Jacobs, editor, Academic Press, London.

Schaeffer, N. and P. Cardin, 2005. Quasigeostrophic model of the instabilities of the Stewartson layer in flat and depth-varying containers. *Physics of Fluids*, **17**, 104111.

Sreenivasan, B. and C.A. Jones, 2006. Azimuthal winds, convection and dynamo action in the polar regions of planetary cores. *Geophys. Astrophys. Fluid Dyn.*, **100**, 319–339.

Thomson, A.W.P. and V. Lesur, 2007. An improved geomagnetic data selection algorithm for global geomagnetic field modelling, *Geophys. J. Int.*, **169**, 951–963, doi:10.1111/j.1365-246X.2007.03354.x.

Tritton, D.J., 1988. *Physical Fluid Dynamics* Oxford Science Publications, Oxford.

Voorhies, C.V., T.J. Sabaka, M. Purucker, 2002. On magnetic spectra of Earth and Mars. *J. Geophys. Res.*, **107(E6)**, 5034, doi:10.1029/2001JE001534.

Whaler, K.A. and R.G. Davis., 1997. Probing the Earth's core with geomagnetism in *Earth's Deep Interior*, 114–166, D.J. Crossley, editor Gordon and Breach, Amsterdam.

Zhang, K., X. Liao, F.H. Busse, 2007. Asymptotic solutions of convection in rapidly rotating non-slip spheres. *J. Fluid Mech.*, **578**, 371–380.

A Divergence-free quasi-geostrophic flows

We search for a velocity field $\mathbf{u}(s,\phi,z)$ defined in the fluid volume (spherical shell of radius r_c), obeying the no-penetration boundary coundition and obtained by adding a small perturbation to a solution of equation (11). The vorticity equation obtained from the equation (14) with the magnetic term omitted yields:

$$\begin{aligned} \frac{\partial}{\partial z} u_s^1 &= 0 \\ \frac{\partial}{\partial z} u_\phi^1 &= 0 \\ u_z^1 &= A(s,\phi,t)z + B(s,\phi,t) \qquad , \end{aligned} \tag{37}$$

where A and B are z-independent. We assume that the velocity field is of the form (37). Then, the impenetrability condition through the boundary $r = r_c$ gives

$$u_z = -\frac{s\,z}{r_c^2 - s^2} u_s \qquad , \tag{38}$$

and, as a result,

$$u_\theta = u_s \frac{\sqrt{s^2+z^2}}{z} \qquad . \tag{39}$$

After elementary transformations, we can write

$$\nabla_H \cdot \mathbf{u} = \nabla_E \cdot \mathbf{u} + \frac{s}{z^2} u_s \tag{40}$$

where $\nabla_E \cdot$ is the equatorial divergence operator $\nabla_E = \nabla - \hat{\mathbf{z}}\partial/\partial z$. If we further impose that the flow is incompressible, then

$$\nabla_E \cdot \mathbf{u} = -\frac{\partial}{\partial z} u_z \qquad . \tag{41}$$

This gives, on the core surface,

$$\nabla_H \cdot \mathbf{u}\,(\theta,\phi) = 2\frac{\tan\theta}{r_c} u_\theta(\theta,\phi) \qquad . \tag{42}$$

The factor 2 in the right-hand side of the above equation results from imposing the flow to be incompressible, in addition to the initial conditions $\frac{\partial}{\partial z}u_s \frac{\partial}{\partial z}u_\phi = 0$ and $\frac{\partial}{\partial z}u_z$ uniform in z.

Our approach has been to consider the simplest QG flow that still verifies the non-penetration condition (see section 4):

$$\mathbf{u} = -\hat{\mathbf{z}} \wedge \nabla\Psi(s,\phi) + u_z^1(s,\phi,z)\,\hat{\mathbf{z}} \qquad . \tag{43}$$

Equation (40) can then be transformed, at the core surface, into the equation (26) (the tangential geostrophic condition) of section 4. This flow is, nonetheless, not divergence-free. An alternative to this choice is to further include a component $\mathbf{u}'$ that garantees that the total flow is incompressible. The tangential geostrophic condition should then be replaced by the condition

$$\nabla_H \cdot (\mathbf{u}\cos^2\theta) = 0 \qquad ,$$

equivalent to (42). The computation of a surface flow compatible with this condition on the core surface can be made following a RLS criterion as we do in our study for tangential geostrophy, but using a different regularization norm. Other constraints used as proxies of a comprehensive dynamical model - minimization of the β-effect, of the rate of strain and of the total energy - have to be modified also. But we don't expect significant differences for small scales. As is well known ((Gire & Le Mouël, 1990)), the toroidal kinetic energy density dominates the poloidal energy density for large n, with $s_n^m \sim n^{-2} t_n^m$, and the divergence-free flow condition changes this relation only but by a factor 2 in the right hand side. We can then envisage that, for flows with length scale l in directions perpendicular to the rotation axis small enough to satisfy the condition of validity of quasi-geostrophy $\eta_c\, l/H_c \ll 1$, the distinction between divergence-free and non divergence-free quasi-geostrophic flows vanishes.

B The expression of Ψ at the core surface

As noticed in section 4, the whole QG columnar flow can be derived from the scalar streamfunction $\Psi(s,\phi)$. This is clearly seen in eq. (13), and can be made explicit in eqs. (16) and (20) by writing

$$\begin{aligned} u_z^1\,(s,\phi,z) &= -\frac{z}{H_c^2}\frac{\partial}{\partial\phi}\Psi(s,\phi) \\ u_z^{1\,\pm}\,(s,\phi,z) &= \frac{z \mp (H_i + H_c)}{H_i H_c}\frac{\partial}{\partial\phi}\Psi^\pm(s,\phi) \qquad . \end{aligned}$$

Being z-independent, Ψ can be expressed in terms of the core surface flow coefficients. What is more, using the tangential geostrophic condition makes it possible to relate Ψ to only the poloidal and zonal toroidal CMB flow coefficients. From (23) and (24)

$$\nabla_H \cdot \mathbf{u}_H = \frac{1}{r_c^2 \cos^2\theta} \frac{\partial}{\partial\phi} \Psi(\theta,\phi)$$
$$\nabla_H \cdot \mathbf{u}_H^{\pm} = \frac{1}{r_c^2 \cos^2\theta} \frac{\partial}{\partial\phi} \Psi^{\pm}(\theta,\phi) \qquad ,$$

making possible to determine the non-zonal coefficients of the streamfunction Ψ in terms of the poloidal coefficients of the CMB flow. The zonal coefficients can be deduced from

$$u_\phi^{zon} = -\frac{1}{r_c \cos\theta} \frac{d}{d\theta} \Psi^{zon}(\theta)$$
$$u_\phi^{\pm\, zon} = -\frac{1}{r_c \cos\theta} \frac{d}{d\theta} \Psi^{\pm\, zon}(\theta) \qquad .$$

As we compute one single set of coefficients for the flow solution, that are expected to describe the flow everywhere on the CMB (whether inside or outside the rim of the TC), the same set of spherical harmonic coefficients is used to describe Ψ and $\Psi^{\pm}$ at the core surface. We denote them by $\{\psi_n^{m,c}, \psi_n^{m,s}\}$. As expected from expressions (23) and (24), we obtain for these coefficients, expressions similar to those relating the geostrophic pressure spherical harmonic coefficients to the poloidal and zonal toroidal surface flow coefficients (e.g., Gire & Le Mouël (1990)):

$$r_c^{-2}\, \psi_n^{m,c(s)} = \underset{(-)}{+} a_n^m\, s_{n-2}^{m,s(c)} \underset{(-)}{+} b_n^m\, s_n^{m,s(c)} \underset{(-)}{+} c_n^m\, s_{n+2}^{m,s(c)}$$
$$r_c^{-2}\, \psi_n^0 = \frac{n-1}{2n-1}\, t_{n-1}^0 + \frac{n+2}{2n+3}\, t_{n+1}^0 \qquad , \tag{44}$$

where

$$a_n^m = \frac{(n-2)(n-1)}{(2n-3)(2n-1)} \frac{\sqrt{(n-m-1)(n-m)(n+m-1)(n+m)}}{m}$$
$$b_n^m = \frac{n(n+1)}{m(2n+1)} \left[\frac{(n-m+1)(n+m+1)}{2n+3} + \frac{(n+m)(n-m)}{2n-1} \right]$$
$$c_n^m = \frac{(n+2)(n+3)}{(2n+5)(2n+3)} \frac{\sqrt{(n-m+1)(n-m+2)(n+m+1)(n+m+2)}}{m}$$

The relations above can be used to write any condition on Ψ or on its latitudinal or meridional derivatives at the CMB, in the form of corresponding conditions on the CMB flow poloidal and zonal toroidal coefficients.

Table 1: Characterization of QG flow $\hat{\mathbf{x}}_1$ using 'pessimistic' errors

	Attenuation parameters		Misfit		Error $K\,\alpha^n$		Physical quantities			
Epoch	λ_{e1}	λ_{e2}	χ_1	χ_2	K	α	$v_{RMS}^{(S)}$ (km/yr)	$v_{RMS}^{(V)}$ (km/yr)	β_{effect} (yr^{-2})	e_{effect} (yr^{-1})
2001.0	2.7×10^4	1.4×10^5	0.98	1.01	4.6	0.6	16.6	9.7	8.8×10^{-10}	5.8×10^{-2}
2002.5	2.0×10^4	6.0×10^4	0.98	1.00	5.9	0.6	17.3	9.6	1.1×10^{-9}	6.5×10^{-2}
2004.0	2.3×10^4	9.0×10^4	1.00	0.98	6.2	0.6	16.8	9.2	9.7×10^{-10}	5.8×10^{-2}

Table 2: Characterization of QG flow $\hat{\mathbf{x}}_1$ using 'optimistic' errors

	Attenuation parameters		Misfit		Error $K\,\alpha^n$		Physical quantities			
Epoch	λ_{e1}	λ_{e2}	χ_1	χ_2	K	α	$v_{RMS}^{(S)}$ (km/yr)	$v_{RMS}^{(V)}$ (km/yr)	β_{effect} (yr^{-2})	e_{effect} (yr^{-1})
2001.0	1.2×10^4	5.3×10^4	1.01	0.99	5.8	0.6	19.3	11.5	1.2×10^{-9}	8.3×10^{-2}
2002.5	1.5×10^4	4.9×10^4	0.99	0.98	6.5	0.6	18.2	10.1	1.2×10^{-9}	7.2×10^{-2}
2004.0	1.3×10^4	6.5×10^4	1.00	0.98	6.9	0.6	18.6	10.4	1.1×10^{-9}	7.3×10^{-2}

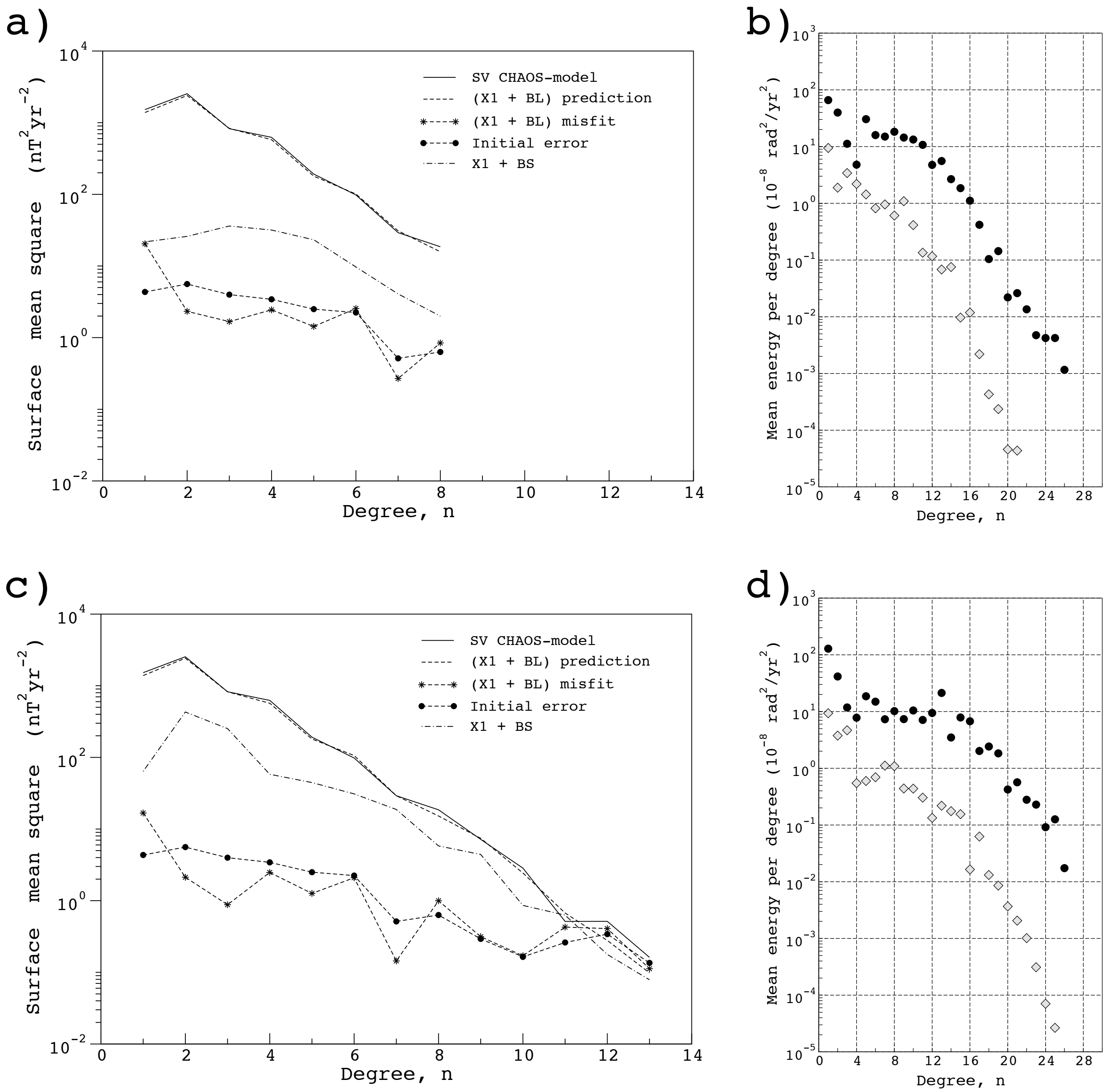

Figure 1: Results from a single inversion of the first 8 degrees (a) and b)) and the first 13 degrees (c) and d)) of CHAOS model at epoch 2001.0, for a tangentially geostrophic CMB flow, using a strong surface regularization. a) and c): Power spectra, at the Earth's surface, of the observed (solid) and the estimated (dashed) SV field, the SV uncertainties used in $\mathbf{C_y}$ (dash-circle), the final differences from the input model (dash-star) and the signal due to advection of BS by the estimated flow $\hat{\mathbf{x}}_1$ (dotted-dashed). b) and d): Mean energy per degree, for toroidal (black circles) and poloidal (grey diamonds) SH components of the CMB flow.

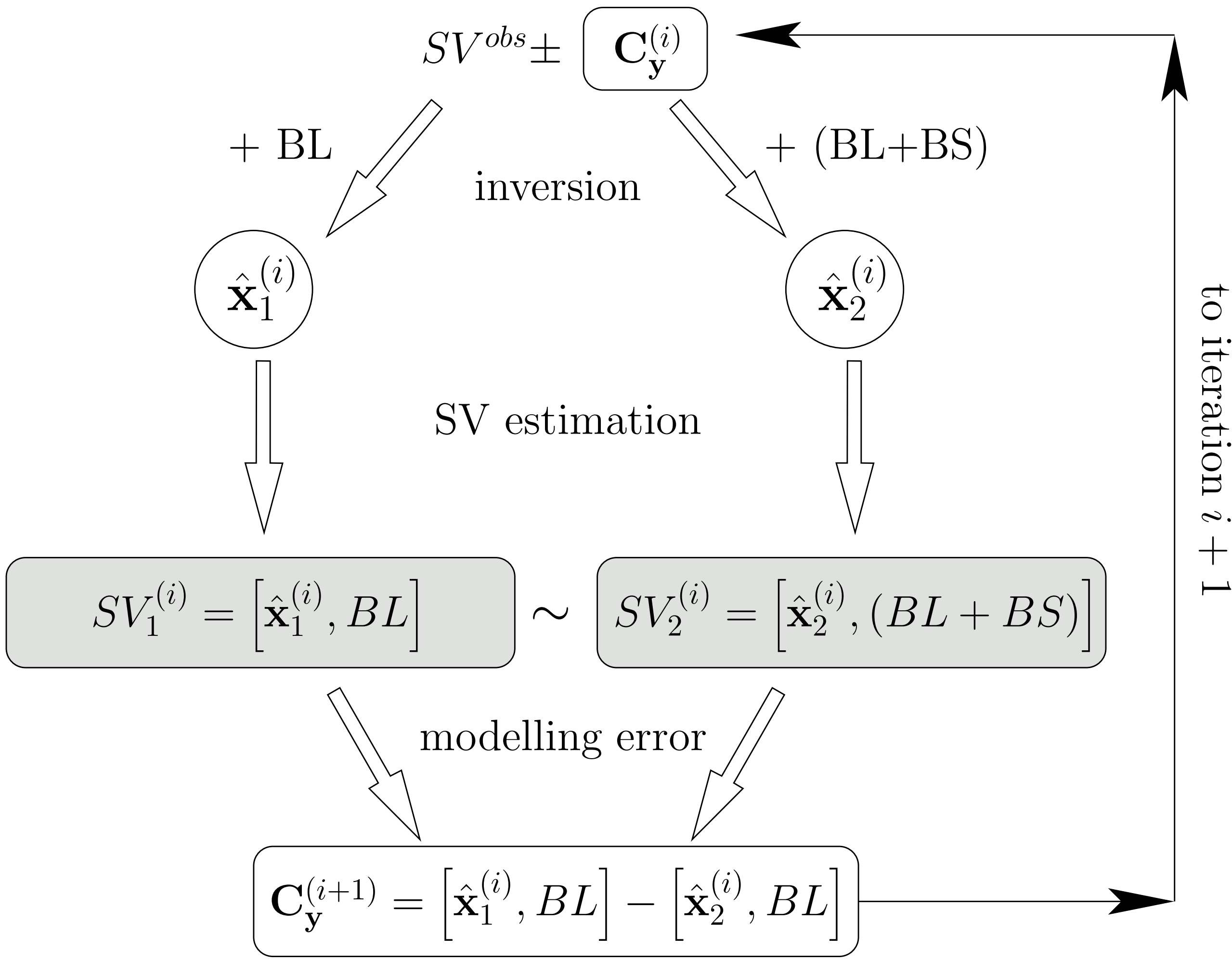

Figure 2: Flowchart to illustrate the iterative method whereby the modelling error due to the interaction between velocity models and the small scale magnetic field is estimated. Here, $[\hat{\mathbf{x}}, B]$ denotes advection of the main field B by the flow $\hat{\mathbf{x}}$.

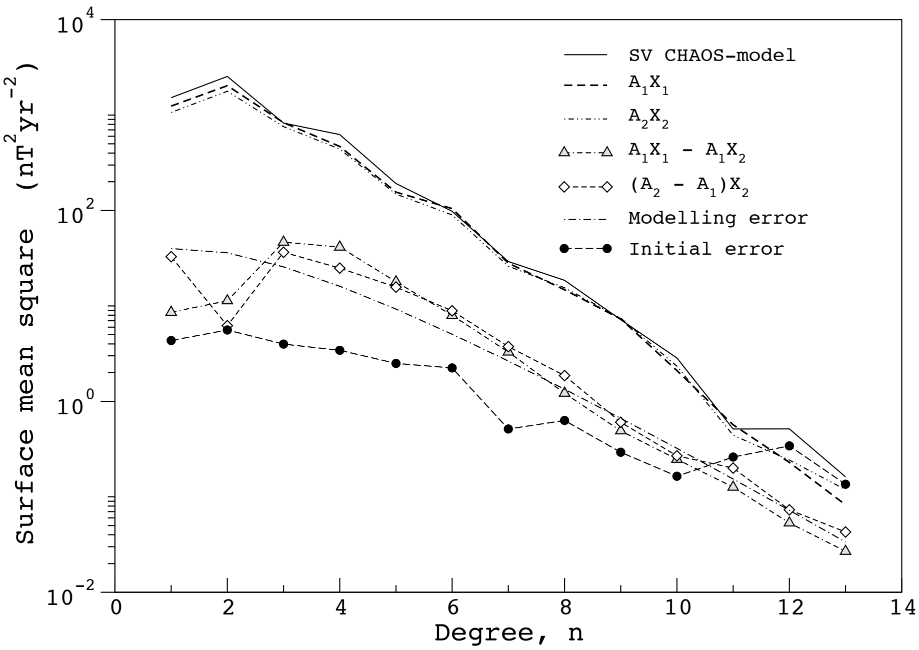

Figure 3: Iterative inversion of the first 13 degrees of CHAOS model at epoch 2001.0, for a tangentially geostrophic flow using strong surface regularization. SV power spectra at the core surface of starting model (solid line), prediction from inverted flow $\hat{\mathbf{x}}_1$ (dashed line) and prediction from inverted flow $\hat{\mathbf{x}}_2$ (dotted-dotted-dashed line). Also represented, the SV uncertainties (black circles), the modelling error estimated at the first iteration (triangles and diamonds) and the converged modelling error (dotted-dashed line).

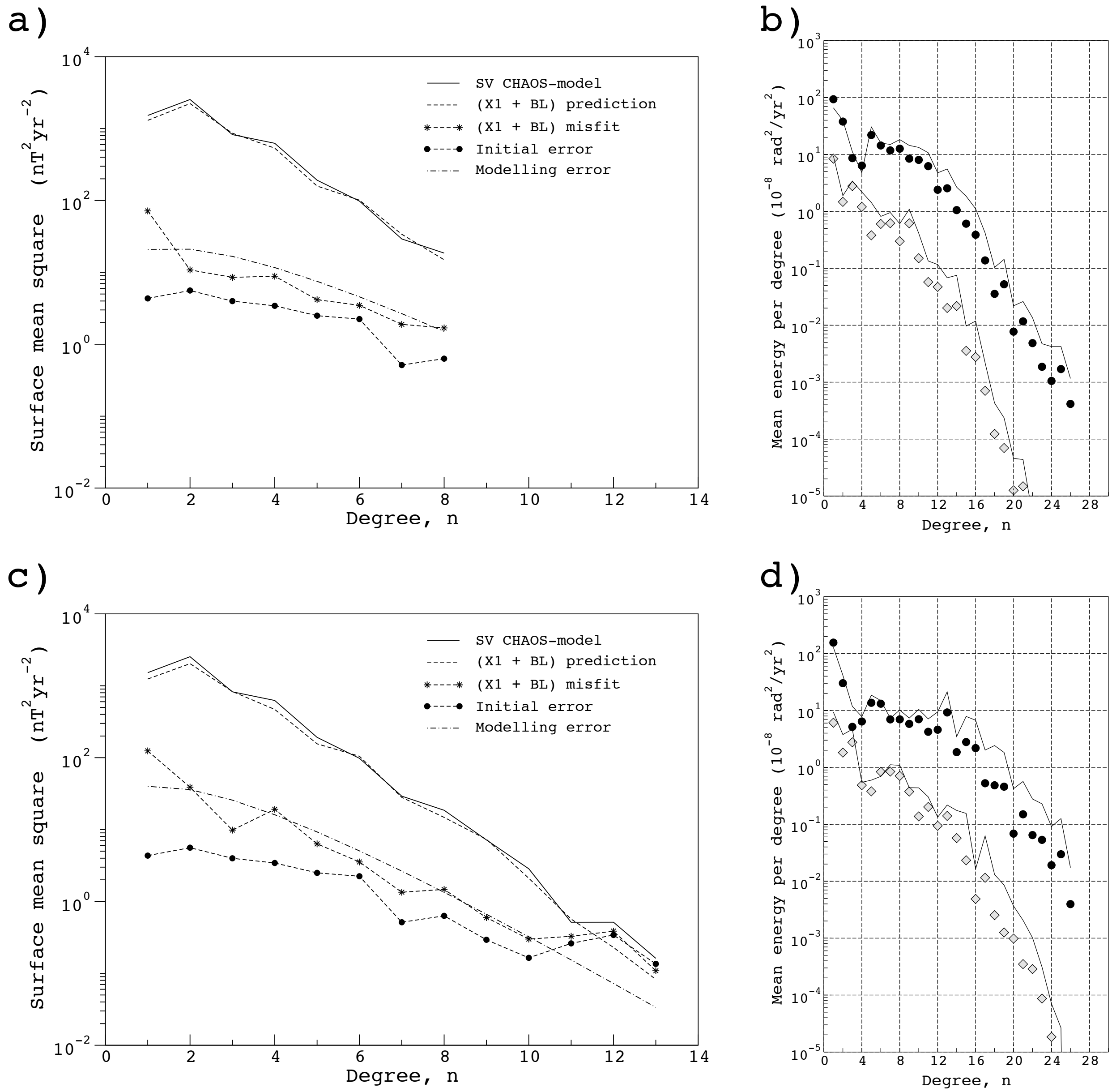

Figure 4: Results from the iterative inversion of the first 8 degrees (a) and b)) and the first 13 degrees (c) and d)) of CHAOS model at epoch 2001.0, for a tangentially geostrophic CMB flow, using a strong surface regularization. a) and c): Power spectra, at the Earth's surface, of the observed (solid) and the estimated (dashed) SV field, the SV uncertainties used in $\mathbf{C_y}$ (dash-circle), the final differences from the input model (dash-star) and the converged modelling error (dotted-dashed). b) and d): Mean energy per degree, for toroidal (black circles) and poloidal (grey diamonds) SH components of the CMB flow, and the corresponding values shown in Figures 1 b) and d) (solid curves), obtained without taking into account modelling errors.

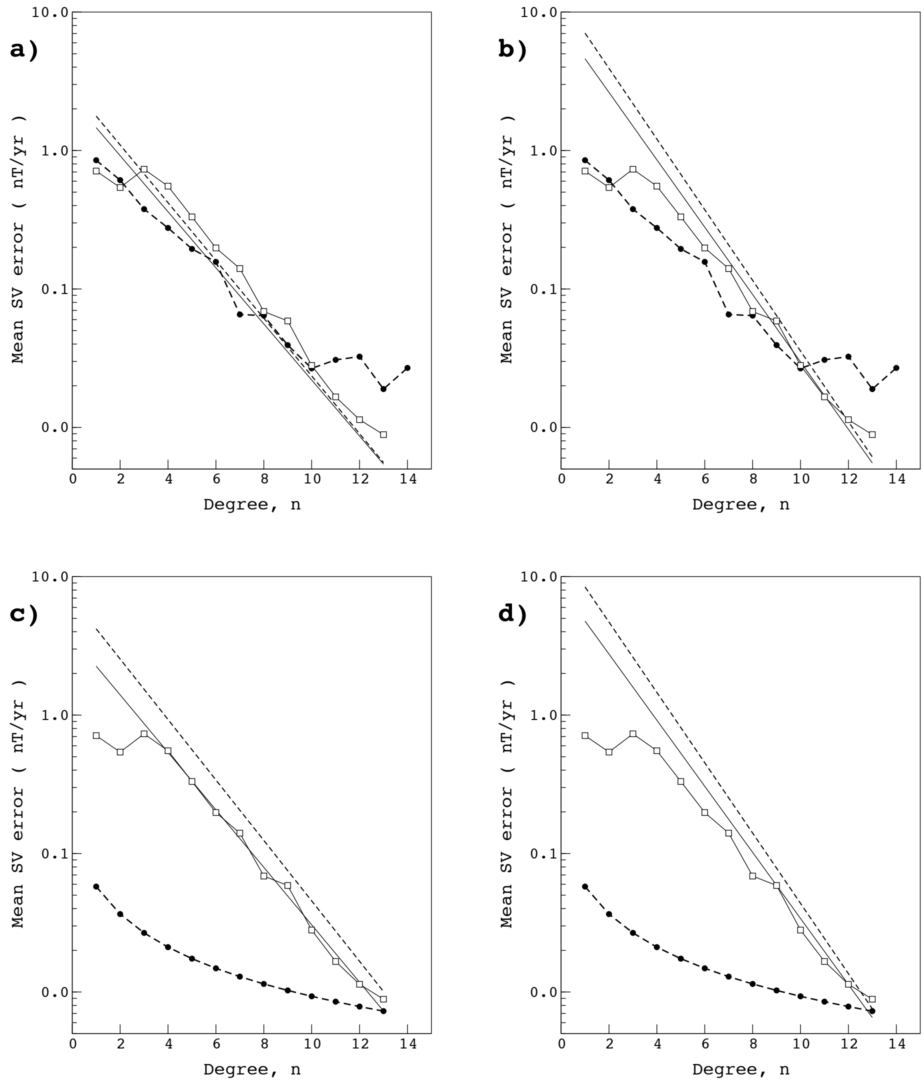

Figure 5: Mean SV errors per degree, at the Earth's surface, in an iterative inversion for tangentially geostrophic flows, using a 'strong-norm' regularization (figures a) and c)) or the minimization of the kinetic energy of the surface flow (figures b) and d)). Shown, are the truncation modelling errors in the first (dashed) and last (solid) iterations, the initially specified SV errors (black circles), 'pessimistic' in figures a) and b) and 'optimistic' in figures c) and d) and the $l = n$ diffusion modelling errors (white squares).

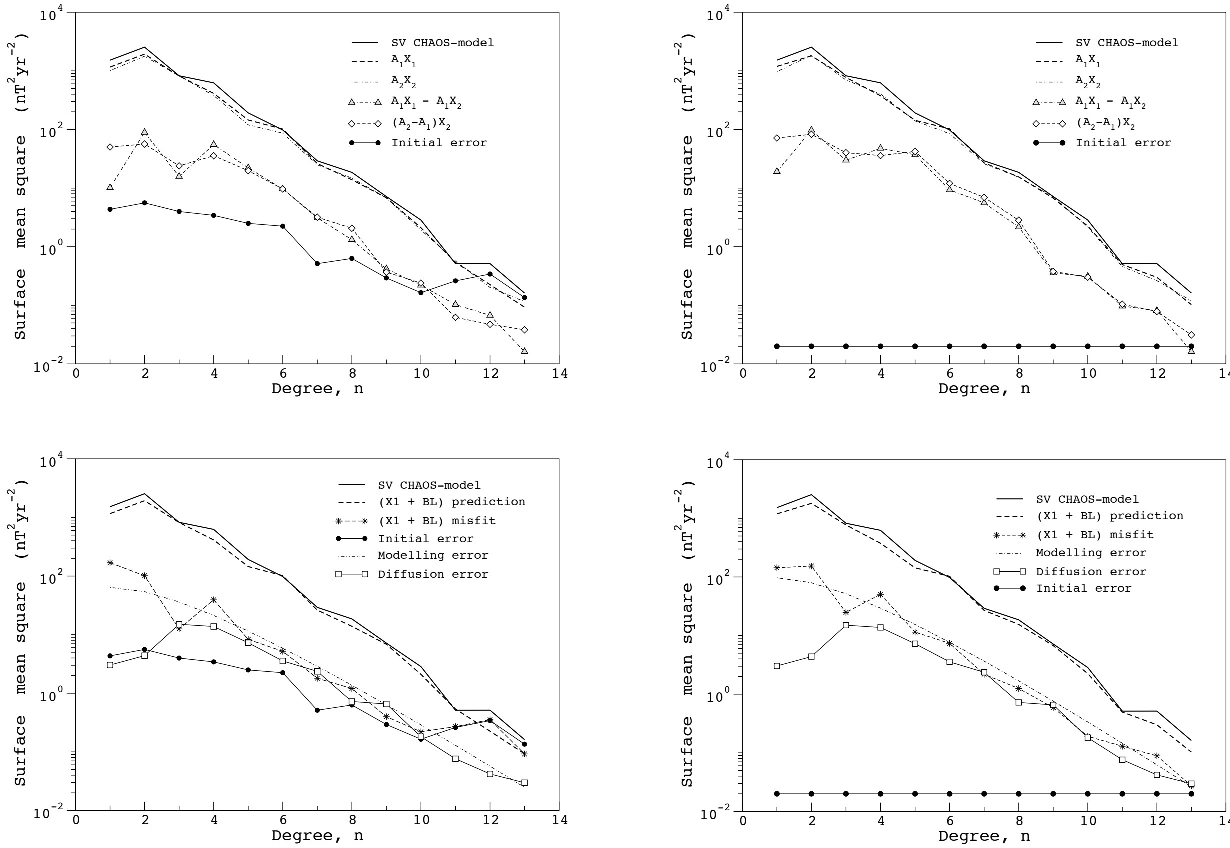

Figure 6: Results from iterative inversion of CHAOS model at epoch 2001.0 for a QG core flow, using new regularization norms specified in section 5. Power spectra at the Earth's surface of different signals specified in the figure legend-box, when starting from 'optimistic' (right column) or 'pessimistic' (left column) SV uncertainties.

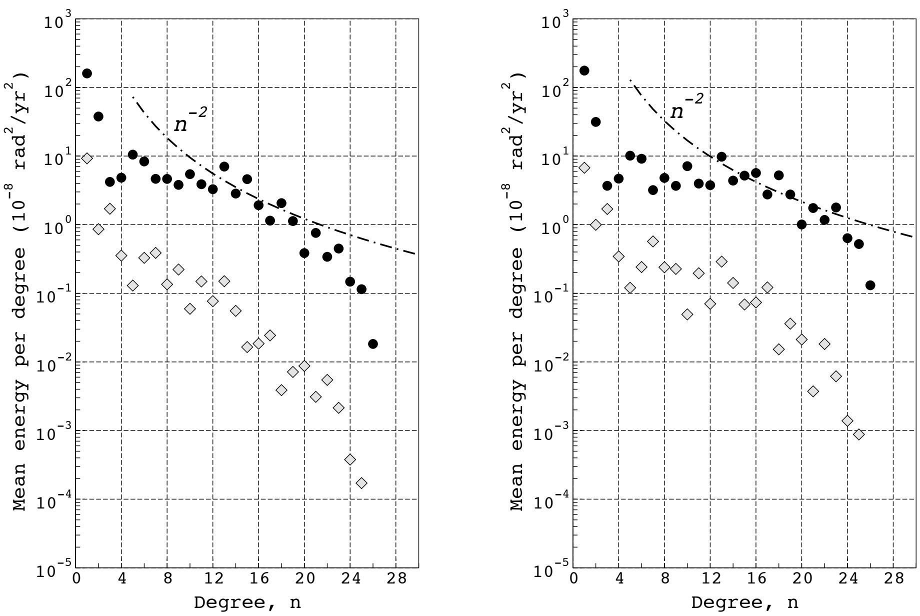

Figure 7: Mean energy per degree for toroidal (black circles) and poloidal (grey diamonds) coefficients of the CMB surface expression of the inverted QG flow for epoch 2001.0. Also shown, the mean energy per degree for a n^{-2} flow spectrum (dotted-dashed curve). Left: 'pessimistic' SV error model. Right: 'optimistic' SV error model.

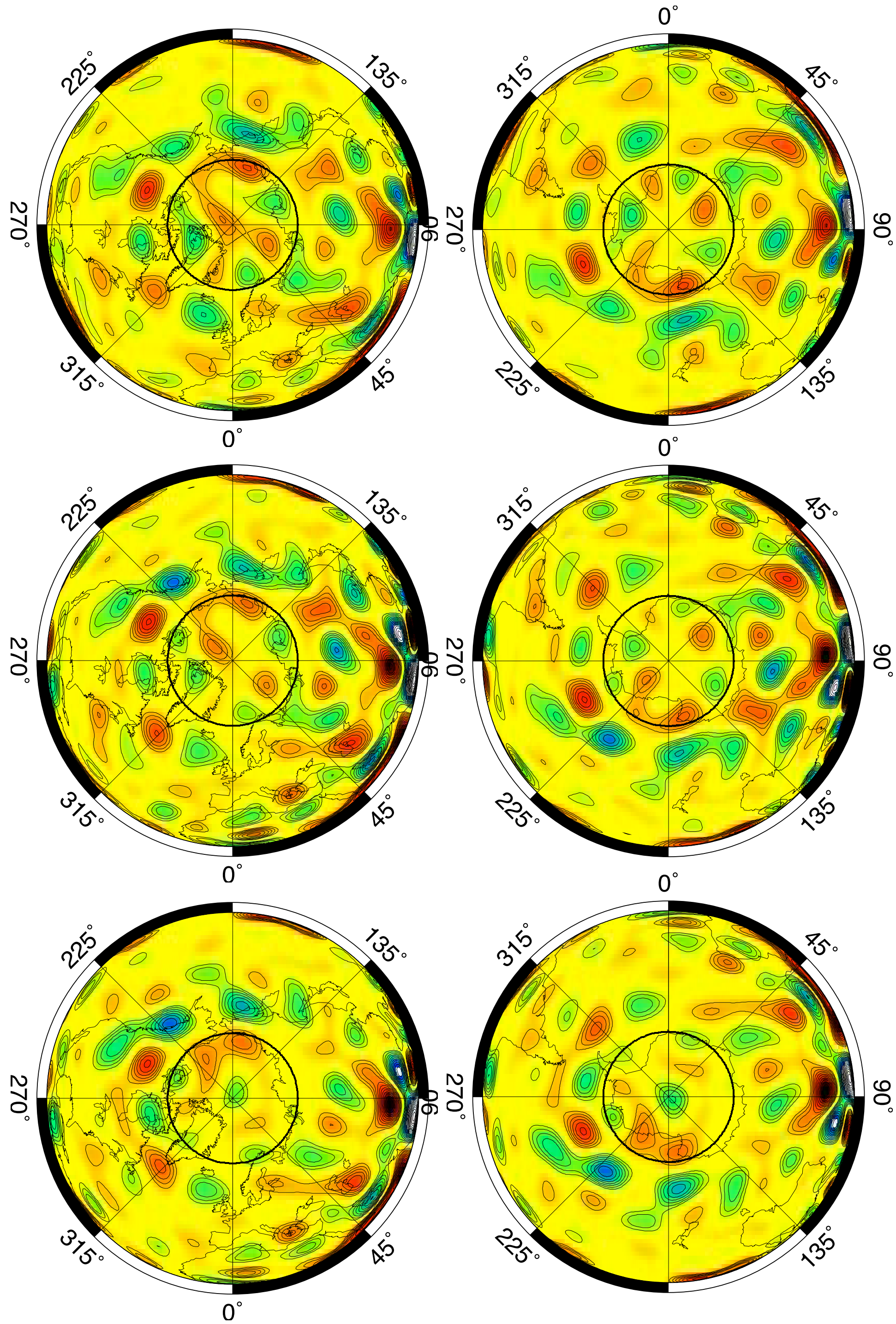

Figure 8: Axial vorticity in the equatorial plane for QG flows obtained from iterative inversion of CHAOS model at epoch 2001.0 (top), 2002.5 (center), 2004.0 (bottom), as viewed from the North (left) and the South (right) poles. Also shown, the projection of the tangent cylinder. Values obtained with the 'pessimistic' initial SV uncertainties. Color scale ranges between -0.25 and +0.25 rad/yr, blue for positive vorticity (cyclones) and red for negative vorticity (anticyclones). Solid line contours only for vorticity intensity between 0.075 and 1.0 rad/yr, every 0.025 rad/yr.

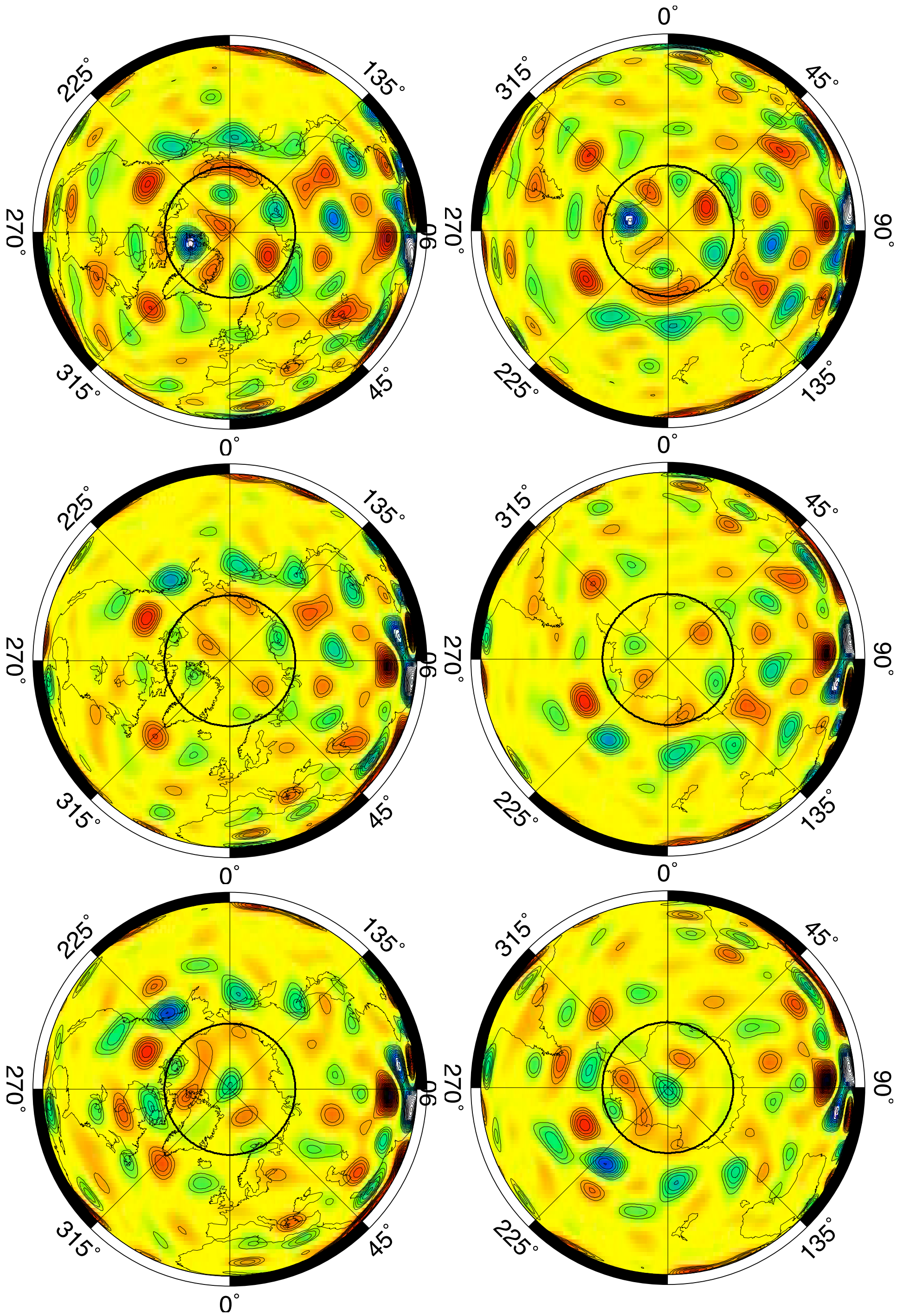

Figure 9: Same as Figure 8, starting from the 'optimistic' initial uncertainties. Color scale ranges between -0.30 and +0.30 rad/yr. Solid line contours only for vorticity intensity between 0.1 and 1.0 rad/yr, every 0.03 rad/yr.

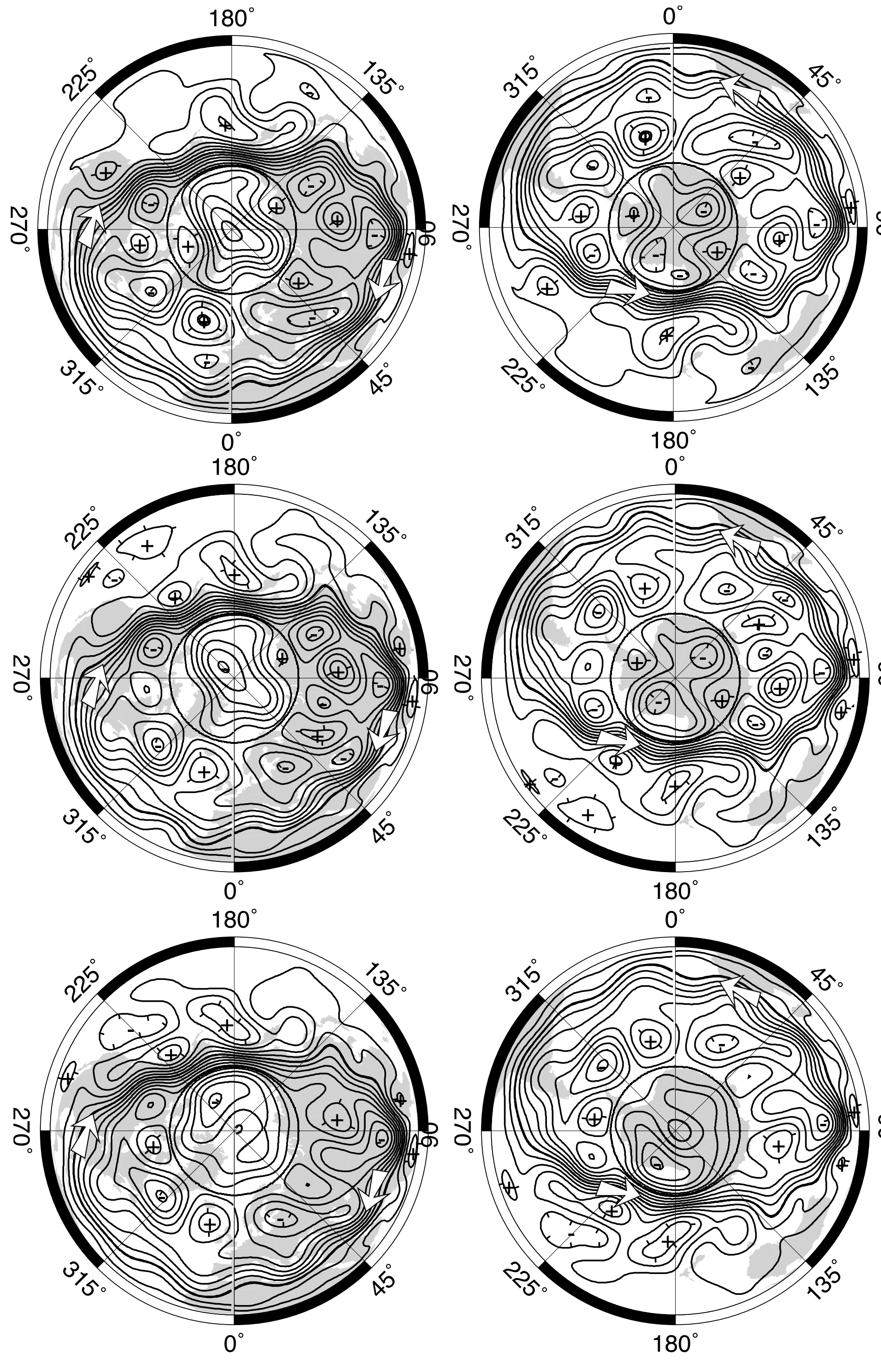

Figure 10: Streamfunction contours at the equatorial plane, for the QG flows obtained from iterative inversion of the CHAOS model at epochs 2001.0 (top), 2002.5 (center), 2004.0 (bottom), as viewed from the North (left) and the South (right) poles. Also shown, the solid core limits. Values, obtained with the 'pessimistic' initial SV uncertainties, range between -6 and +6 km/yr. Flow circulation is westward along the large jet feature and is cyclonic (+) or anticyclonic (-) in vortices.

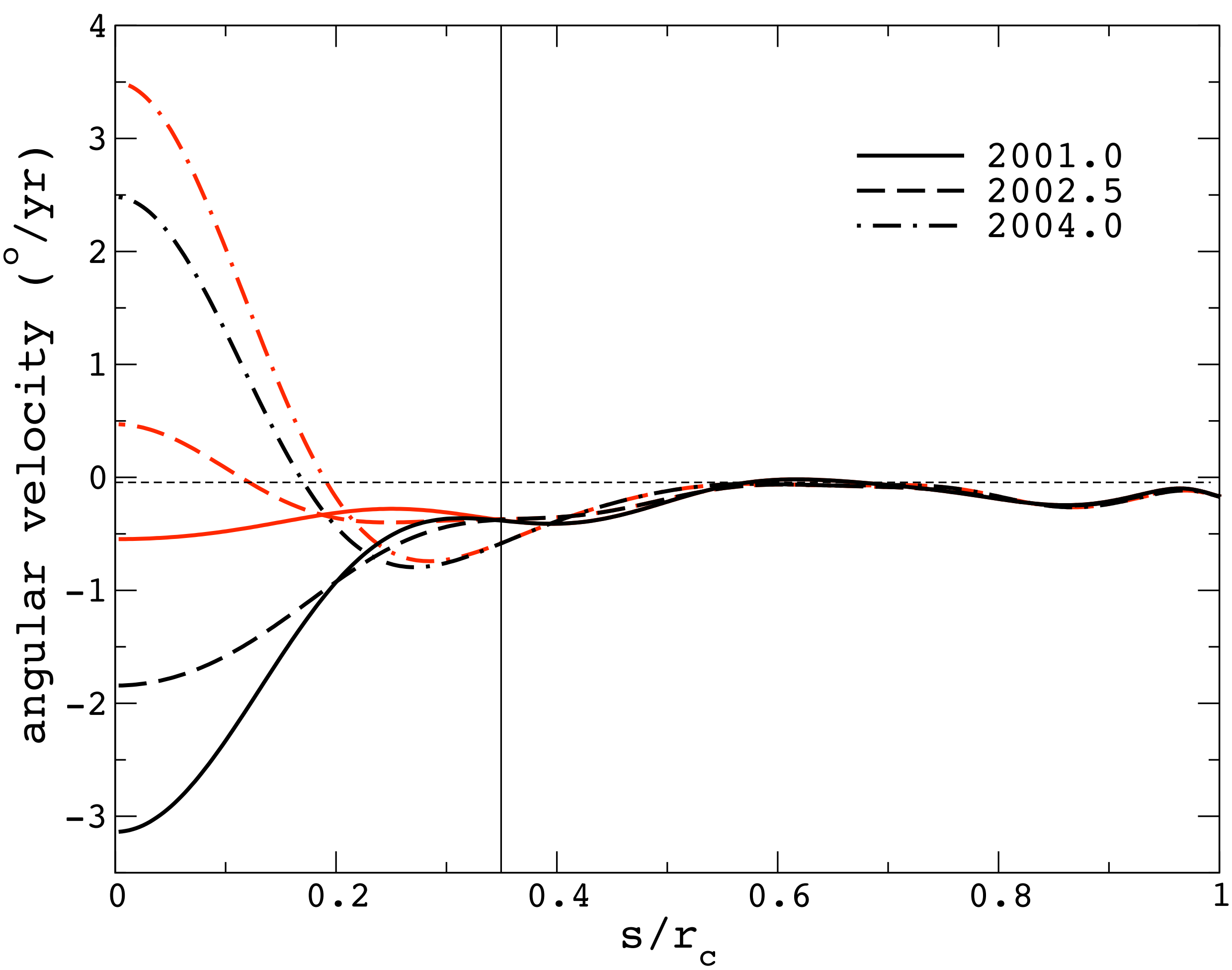

Figure 11: Zonal angular velocity as a function of normalized distance to rotation axis, for QG flows inverted from CHAOS model at epochs 2001.0 (solid), 2002.5 (dashed) and 2004.0 (dotted-dashed), using ‘pessimistic’ initial SV uncertainties. Also shown the inner core radius, below which black and red curves refer to the Northern and to the Southern hemispheres, respectively.

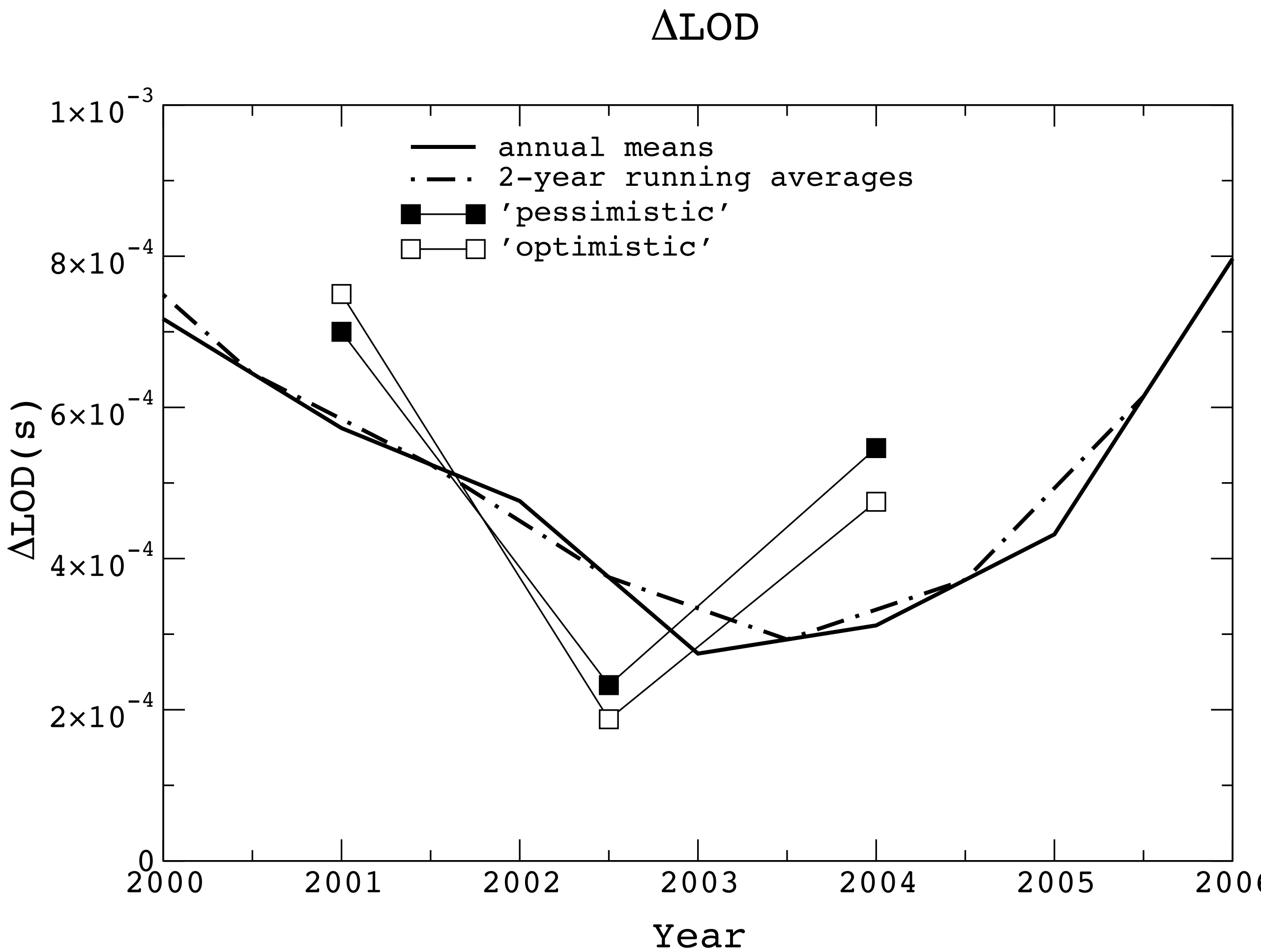

Figure 12: Observed (solid and dotted-dashed lines) and predicted (squares) excess length-of-day. Predictions are from QG flows inverted iteratively from CHAOS model, for epochs 2001.0, 2002.5 and 2004.0.

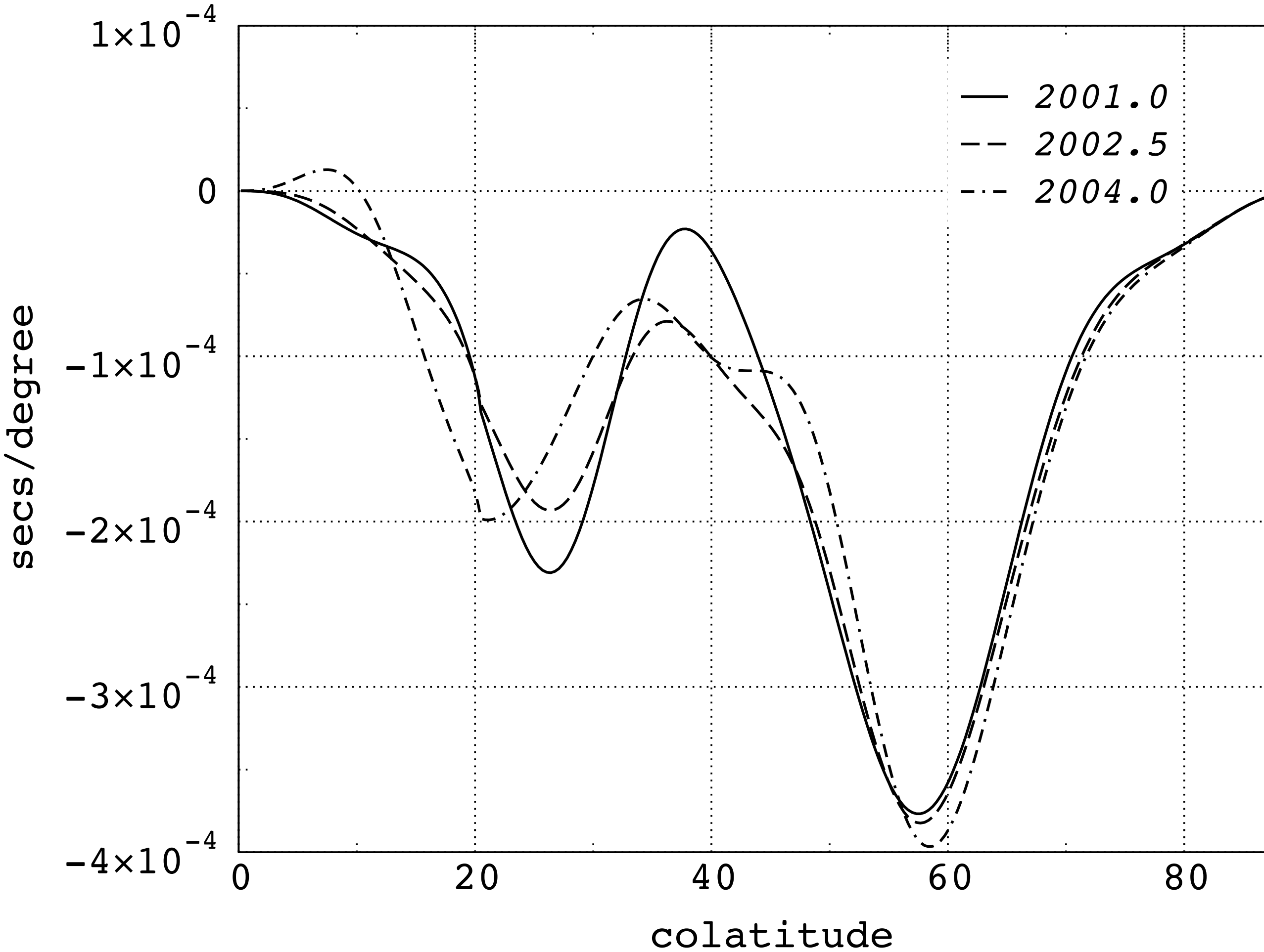

Figure 13: Distribution of the contribution per degree of latitude, to excess length of day of the liquid core divided into coaxial cylindrical annuli. Results using 'pessimistic' initial SV uncertainties.